

Rapid and accurate parameter inference for coalescing, precessing compact binaries

J. Lange,¹ R. O’Shaughnessy,¹ and M. Rizzo¹

¹*Center for Computational Relativity and Gravitation, Rochester Institute of Technology, Rochester, New York 14623, USA*

Extending prior work by Pankow et al, we introduce RIFT, an algorithm to perform Rapid parameter inference on gravitational wave sources via Iterative FiTting. We demonstrate this approach can correctly recover the parameters of coalescing compact binary systems, using detailed comparisons of RIFT to the well-tested LALInference software library. We provide several examples where the unique speed and flexibility of RIFT enables otherwise intractable or awkward parameter inference analyses, including (a) adopting either costly and novel models for outgoing gravitational waves; and (b) mixed approximations, each suitable to different parts of the compact binary parameter space. We demonstrate how RIFT can be applied to binary neutron stars, both for parameter inference and direct constraints on the nuclear equation of state.

I. INTRODUCTION

The Advanced LIGO [1] and Virgo [2] ground-based gravitational wave (GW) detectors have identified several coalescing compact binaries [3–8]. Over the next few years, hundreds more will be confidently identified, with proportionally more uncertain candidates at the margins of detector sensitivity. These sources provide an opportunity and a challenge. On the one hand, reliable, unbiased parameter inferences will be essential to achieve the full potential of high-precision tests of general relativity; constraints on nuclear matter; and inferences about present-day populations and progenitor astrophysics. On the other hand, these inferences will be stable only with a careful exploration of model systematics, which at present cannot be performed due to their computational cost. For example, using the standard parameter estimation pipeline LALInference (LI) [9], only special-purpose approximations and infrastructure can enable generic analyses with computational costs measured in less than days (for binary black holes) or weeks (for binary neutron stars) and simultaneously produce production-ready results which comprehensively estimate all binary parameters.

To address this challenge, Pankow et al. [10] proposed an alternative and highly-parallelizable grid-based parameter estimation strategy. In this approach, each candidate GW signal is compared to a regular grid of candidate source parameters, producing an array of candidate likelihood values, a process henceforth denoted by ILE. Interpolating the likelihood over the grid, Pankow et al [10] estimated the masses of low-mass compact objects. Since the original study, several investigations have applied a similar method to other masses and higher dimension [11–13]. Due to the exponentially-increasing number of points appearing in a regular grid in high dimension, these later approaches usually adopted a different approach for analyzing strong signals, approximating the likelihood by a Gaussian in suitable coordinates.

In this work, building on early changes adopted in [13], we introduce and demonstrate a straightforward generalization of the approach in Pankow et al. To circumvent the cost and limitations of polynomial interpolation and periodic grids, we perform gaussian process interpolation on an unstructured grid. Further, to create and validate the grid used for interpolation, we employ an iterative procedure, using estimates of the posterior distribution at stage k to propose new grid

points to augment generation $k + 1$. We demonstrate this procedure can rapidly and accurately recover the parameters of generic quasicircular binaries, including models and scenarios whose computational cost would be prohibitive for LI. This approach has been developed and applied to GW observations since 2016, particularly in the context of comparisons to numerical relativity.

This paper is organized as follows. In Section II we describe our parameter estimation pipeline, including the underlying gaussian process interpolation; iterative evaluation of ILE on the posterior grid; and convergence tests. In Section III we enumerate the concrete models used for parameter inference in this work. In Section IV we describe several validation studies we performed to assess it, including purely synthetic likelihoods and head-to-head comparison with LI. In Section V we describe applications of our pipeline, particularly to assessing the impact of model systematics. We summarize our results and discuss future generalizations in Section VII. In a companion paper [14], we demonstrate how the likelihood fitting techniques developed in this work can be applied to direct comparison of GW measurements with solutions of Einstein’s equations, as in [11, 12].

II. PARAMETER INFERENCE VIA ITERATIVE GAUSSIAN PROCESS FITS

A. Coordinates and notation

A coalescing compact binary in a quasicircular orbit can be completely characterized by its intrinsic parameters, namely its individual masses m_i , spins \mathbf{S}_i , and by internal multipole moments which characterize its matter degrees of freedom like the individual dimensionless tidal deformabilities Λ_i (see Appendix A 3); and its seven extrinsic parameters: right ascension, declination, luminosity distance, coalescence time, and three Euler angles characterizing its orientation (e.g., inclination, orbital phase, and polarization). In this work, we will also use the total mass $M = m_1 + m_2$ and mass ratio q defined in the following way:

$$q = m_1/m_2, \text{ where } m_1 > m_2. \quad (1)$$

With regard to spin, we define an effective spin [15–17], which is a combination of the spin components along to or-

bital angular momentum, in the following way,

$$\chi_{\text{eff}} = (\mathbf{S}_1/m_1 + \mathbf{S}_2/m_2) \cdot \hat{L}/M \quad (2)$$

where \mathbf{S}_1 and \mathbf{S}_2 are the dimensionless spins on the individual BH defined:

$$\chi_i = \mathbf{S}_i/m_i^2. \quad (3)$$

We will express the dimensionless spins in terms of cartesian components $\chi_{i,x}, \chi_{i,y}, \chi_{i,z}$, expressed relative to a frame with $\hat{z} = \hat{L}$ and (for simplicity) at the orbital frequency corresponding to the earliest time of astrophysical interest (e.g., an orbital frequency of $\simeq 10\text{Hz}$).

B. Marginalized likelihoods

ILE provides a straightforward and efficient mechanism to compare any specific candidate gravitational wave source with real or synthetic data [10–13], by marginalizing the likelihood of the data over the seven coordinates characterizing the binary’s coalescence event and orientation relative to the earth. Specifically the likelihood of the data given gaussian noise has the form (up to normalization)

$$\ln \mathcal{L}(\boldsymbol{\lambda}; \theta) = -\frac{1}{2} \sum_k \langle h_k(\boldsymbol{\lambda}, \theta) - d_k | h_k(\boldsymbol{\lambda}, \theta) - d_k \rangle_k - \langle d_k | d_k \rangle_k, \quad (4)$$

where h_k are the predicted response of the k^{th} detector due to a source with parameters $(\boldsymbol{\lambda}, \theta)$ and d_k are the detector data in each instrument k ; $\boldsymbol{\lambda}$ denotes the combination of redshifted mass M_z and the remaining parameters needed to uniquely specify the binary’s dynamics; θ represents the seven extrinsic parameters (4 spacetime coordinates for the coalescence event and 3 Euler angles for the binary’s orientation relative to the Earth); and $\langle a|b \rangle_k \equiv \int_{-\infty}^{\infty} 2df \tilde{a}(f) \tilde{b}^*(f) / S_{h,k}(|f|)$ is an inner product implied by the k^{th} detector’s noise power spectrum $S_{h,k}(f)$. In practice we adopt a low-frequency cut-off f_{min} so all inner products are modified to

$$\langle a|b \rangle_k \equiv 2 \int_{|f| > f_{\text{min}}} df \frac{\tilde{a}(f) \tilde{b}^*(f)}{S_{h,k}(|f|)}. \quad (5)$$

The joint posterior probability of $\boldsymbol{\lambda}, \theta$ follows from Bayes’ theorem:

$$p_{\text{post}}(\boldsymbol{\lambda}, \theta) = \frac{\mathcal{L}(\boldsymbol{\lambda}, \theta) p(\theta) p(\boldsymbol{\lambda})}{\int d\boldsymbol{\lambda} d\theta \mathcal{L}(\boldsymbol{\lambda}, \theta) p(\boldsymbol{\lambda}) p(\theta)}, \quad (6)$$

where $p(\theta)$ and $p(\boldsymbol{\lambda})$ are priors on the (independent) variables $\theta, \boldsymbol{\lambda}$. For each $\boldsymbol{\lambda}$, we evaluate the marginalized likelihood

$$\mathcal{L}_{\text{marg}} \equiv \int \mathcal{L}(\boldsymbol{\lambda}, \theta) p(\theta) d\theta \quad (7)$$

via direct Monte Carlo integration, where $p(\theta)$ is uniform in 4-volume and source orientation. To evaluate the likelihood in regions of high importance, we use an adaptive Monte

Carlo as described in [10]. As described in Pankow et al, this marginalized likelihood can be evaluated efficiently because, having generated the dynamics and outgoing radiation in all possible directions once and for all for fixed $\boldsymbol{\lambda}$, the likelihood can be evaluated as a function of θ at very low computational cost.

Using Bayes’ theorem, the posterior distribution for intrinsic parameters $\boldsymbol{\lambda}$ can be expressed as

$$p_{\text{post}} = \frac{\mathcal{L}_{\text{marg}}(\boldsymbol{\lambda}) p(\boldsymbol{\lambda})}{\int d\boldsymbol{\lambda} \mathcal{L}_{\text{marg}}(\boldsymbol{\lambda}) p(\boldsymbol{\lambda})}. \quad (8)$$

where prior $p(\boldsymbol{\lambda})$ is the prior on intrinsic parameters like mass and spin. ILE itself will only provide point estimates $\ln \mathcal{L}_{\text{marg}\alpha}$ given proposed evaluation points $\boldsymbol{\lambda}_\alpha$, not the interpolated $\ln \mathcal{L}_{\text{marg}}$ necessary to construct a full solution.

C. Gaussian process interpolation

Given some proposed training data $\{(\boldsymbol{\lambda}_\alpha, \ln \mathcal{L}_{\text{marg}\alpha})\}$, we estimate $\ln \mathcal{L}_{\text{marg}}$ via conventional Gaussian Process interpolation [18] to produce a weakly nonparametric interpolation and error estimate. Gaussian process interpolation has already been used in the field [13, 13, 19–22], particularly to propagate uncertainties. In this approach, we estimate the expected value of $y(x)$ from data x_* and values y_* via

$$\langle y(x) \rangle = \sum_{\alpha, \alpha'} k(x, x_{*,\alpha}) (K^{-1})_{\alpha, \alpha'} y_{*,\alpha'} \quad (9)$$

where α is an integer running over the number of training samples in (x_*, y_*) and where the matrix $K = k(x_\alpha, x'_\alpha) y_*$. [For brevity and to be consistent with conventional notation, in this section we denote $\boldsymbol{\lambda}_\alpha$ by x and $\ln \mathcal{L}_{\text{marg}\alpha}$ by y .] We employ a kernel function $k(x, x')$ which allows for uncertainty in each estimated training point’s value $y_{*,\alpha}$ due to Monte Carlo integration, as well as a conventional squared exponential kernel to allow for changes in the functions versus parameters:

$$k(x, x') = \sigma_o^2 e^{-(x-x')Q(x-x')/2} + \sigma_n^2 \delta_{x,x'} \quad (10)$$

Following usual practice and to insure flexibility for generic sources, we optimize the hyper-parameters σ_o, σ_n and the positive-definite symmetric matrix Q on our training data. We perform all gaussian process interpolation with widely-available open-source software [23]. The computational cost of full-scale Gaussian process optimization and evaluation increases rapidly with the dimension D of the matrix K , as D^3 and D^2 respectively; for typical hardware, we are presently limited to $O(10^4)$ training points in 8 dimensions. In future work we will employ other techniques like sparse approximations and multilayer (“pool-of-experts”) designs, which can achieve comparable results with better scaling.

D. Flexible Monte Carlo generation of posterior samples

We use a single code (henceforth denoted by CIP) to Construct the Intrinsic Posterior distribution, by loading train-

ing data $\{(\lambda_\alpha, \ln \mathcal{L}_{\text{marg}\alpha})\}$; fitting that data, using some coordinate system X for $\{\lambda\}$; and then constructing samples from the posterior distribution via adaptive Monte Carlo using another coordinate system Y with fiducial prior distributions $p(y)$, employing the same adaptive Monte Carlo techniques described [10] and applied in ILE. When fitting the likelihood, we employ coordinate systems well-adapted to the likelihood, which based on many decades of theoretical and computational studies are likely to produce an approximately gaussian likelihood in the limit of strong signals (e.g., coordinates in which the Fisher matrix is a good approximation to the log-likelihood in the high-SNR limit). When performing a Monte Carlo integral to construct a posterior distribution, however, we employ coordinates Y that allow us to efficiently specify the priors in separable form and simultaneously sample the parameter space thoroughly in the region with significant prior support. For example, we often use the chirp mass $\mathcal{M} = (m_1 m_2)^{3/5} / (m_1 + m_2)^{1/5}$ as a sampling coordinate, to insure our adaptive Monte Carlo method can efficiently identify the often exceptionally narrow region of \mathcal{M} consistent with the posterior, particularly for binary neutron stars. In Appendix A we describe the specific array of coordinate systems and priors we use.

As with ILE, the adaptive Monte Carlo produces a sequence of weighted points w_k, λ_k that fully characterize the posterior distribution. For example, any one-dimensional marginal distribution for a function $g(\lambda)$ can be computed via the corresponding weighted sum $P(< G) = [\sum_k w_k \Theta(g(\lambda_k) - G)] / \sum_q w_q$, where Θ is the Heavyside function. To improve compatibility with other codes' output and to minimize overhead – in practice, a set of weighted posterior samples often includes $\gg 10^8$ points, many with low weight – we then uniformly resample from the weighted posterior points, with replacement. Specifically, after ordering the sequence w_k so $w_1 \leq w_2 \leq \dots$, we draw N uniformly distributed random numbers u_q and choose λ_q such that q is the largest number with $\sum_{k \leq q} w_k / \sum_k w_k < u_q$.

Our adaptive Monte Carlo procedure currently requires separable priors, as described in Appendix A. We generate results for generic priors by reweighting the underlying weighted samples produced above, before performing the draw-with-replacement procedure to generate a fair sample from the target posterior. For example, if $\{(w_k, \lambda_k)\}$ are generated by the procedure above with a prior $p_{\text{ref}}(\lambda)$, then we generate posterior distributions suitable to a prior $p(\lambda)$ via reweighted samples $\{(w_k p(\lambda_k) / p_{\text{ref}}(\lambda_k), \lambda_k)\}$, following the procedures outlined above.

E. Iterative procedure

The fitting and sampling procedures described above produces a proposed set of posterior samples $B_0 = \{\lambda_k\}$, given training data $A_0 = \{\lambda_\alpha\}$. We then use ILE to evaluate $\ln \mathcal{L}_{\text{marg}}$ on λ_k , then perform the procedure described above starting with revised training data $A_1 = A_0 \cup B_0$ to produce a new set of proposed samples B_1 . By repeating this process several times, we can validate and refine our fit and hence

posterior. To assess whether the fit and posterior have converged, we use (all of) the one-dimensional marginal distributions, comparing the empirical cumulative distributions in one iteration against the next using standard tools; see Appendix B. As described in Appendix B, we tested this iterative fitting and posterior generation procedure using synthetic likelihood functions $\ln \mathcal{L}_{\text{marg}}$ for which the posterior distributions can be calculated analytically. This procedure succeeds consistently for all dimensions we thoroughly tested ($d \leq 6$).

We extended the basic framework described above to make it more robust and efficient. To make the process more robust, we employ a dithering step. Specifically, given (a subset of) B_k and its covariance Σ in the subset of parameters we choose to dither, we can add random offsets $\Delta \lambda_k$ drawn from a multinormal distribution with covariance $\epsilon^2 \Sigma$, where ϵ is a factor controlling the amount of dithering. After removing samples which due to $\Delta \lambda_k$ are no longer physical, we have a new set C_k . The iterative procedure uses both undithered and dithered points, so $A'_{k+1} = A'_k \cup B_k \cup C_k$. We typically employ a dithering factor $\epsilon \simeq 1$. Second, to make the process more efficient, we can (if needed) perform the first several iterations with fewer and physically-motivated degrees of freedom: the map $X(\lambda)$ used to perform the fit will have fewer dimensions than λ . This approach may be required if the initial training set A_0 is too small to provide a useful fit in all dimensions of λ . If the likelihood can be approximated at some level using only the variables in X – if only that subset of variables characterizes the most easily measurable quantities – then these dimensionally-reduced iterations cause the remaining degrees of freedom to be efficiently and randomly explored. As a concrete example, for massive binary black holes like GW150914, even if precessing, the likelihood can be well approximated using just $\mathcal{M}, \eta, \chi_{\text{eff}}$ [11], though after more iterations our fitting procedure captures more subtle features of the fit and hence posterior. After these first few seed iterations, we revert back to the conventional approach described above.

Gaussian processes are expensive, with evaluation cost scaling as the number of points squared. Before fitting, we always eliminated points whose marginalized likelihoods were many orders of magnitude outside the expected support of the distribution (i.e., with $\ln \mathcal{L} \lesssim \ln \mathcal{L}_{\text{max}} - F \chi_d^2(0.9)/2$ where $\chi_d^2(x)$ is the inverse-chisquared distribution with d degrees of freedom, and $F \simeq 10$). In rare cases, even after this condition is applied, we iteratively accumulate a number of points N greater than our computationally-tractable limit N_* . In these cases, we randomly subdivide our training points into G equal-sized subgroups smaller than N_* . In one approach, we repeat our analysis on each random subsample, constructing $b = 1 \dots G$ gaussian-process approximations $g_b(\lambda)$ and posterior samples A_b , requiring consistency between these outputs A_b . In another approach, we construct the posterior distribution using the average $\bar{g}(\lambda) \equiv \sum_b g_b(\lambda) / G$.

As in previous work [10, 11], we analyze data containing candidate signals starting with a good approximation to (some of) that sources' parameters, provided by the search algorithm which flagged this stretch of data as a candidate binary coalescence. We use this information to conservatively identify

the initial grid A_o of test parameters to explore; see, e.g., [10] and references therein.

F. Reconstructing source-frame binary masses

ILE compares waveforms with fixed detector-frame masses $m_{i,z} = m_i(1+z)$ to real and synthetic observational data. As a result, the procedures described above (and in all previous work) produce posterior distributions as a function of $M_z = (m_1 + m_2)(1+z)$ and dimensionless intrinsic variables. We must perform some additional post-processing and analysis to recover the distribution of the total source-frame mass $M = (m_1 + m_2)$ and its joint distribution with all other intrinsic parameters.

The most straightforward and robust procedure to reconstruct the full, joint source-frame posterior reprocesses the output of ILE from the final set of draws A_N from the iterative procedure described above. Each point $\lambda_k \in A_N$ is a fair draw from the posterior distribution, by design. In the process of performing the Monte Carlo integral for $\ln \mathcal{L}_{\text{marg}}$ for each λ_k , ILE produces weighted posterior samples $\{w_{k,\alpha}, \theta_{k,\alpha}\}$, where the parameters $\theta_{k,\alpha}$ include the distance and therefore redshift z . We generate the joint posterior distribution on source-frame parameters by combining all ILE output samples and re-expressing all masses using a suitable redshift. For example, we can generate the cumulative distribution of M via $P(< M) = \sum_{k,\alpha} w_{k,\alpha} \Theta(M - M_{z,k}/(1+z_{k,\alpha}))$.

III. MODELS AND SOURCES IN THIS WORK

In this work, we perform parameter inference with several standard approximations to the outgoing radiation of coalescing binaries, which fall in three families: effective one body (EOB) models [24, 25], specifically SEOBNRV3, SEOBNRV4, and SEOBNRV4.ROM; phenomenological frequency-domain inspiral and merger models, specifically using IMRPHENOMD and IMRPHENOMPv2 [26]; and surrogate waveforms, directly calibrated to numerical relativity [27–29], specifically using NRSur7dq2.

The EOB approach models the inspiral and spin dynamics of coalescing binaries via an ansatz for the two-body Hamiltonian [30], which is solved in the time domain. For nonprecessing binaries, outgoing gravitational radiation during the inspiral phase is generated using an ansatz for resumming the post-Newtonian expressions for outgoing radiation including non-quasicircular corrections, for the leading-order $\ell = 2$ subspace. For the merger phase of nonprecessing binaries, the gravitational radiation is generated via a resummation of many quasinormal modes, with coefficients chosen to ensure smoothness. The final BH’s mass and spin, as well as some parameters in the nonprecessing inspiral model, are generated via calibration to numerical relativity simulations of BBH mergers. For precessing binaries, building off the post-Newtonian ansatz of separation of timescales and orbit averaging [31–34], gravitational radiation during the inspiral

is modeled as if from an instantaneously nonprecessing binary (with suitable nonprecessing spins), in a frame in which the binary is not precessing [35–37]. During the merger, the radiation is approximated using the same final BH state, with the same precession frequency.¹ With well-specified initial data in the time domain, this method can be directly compared to the trajectories [39] and radiation [40] of numerical BBH spacetimes. In this work we use SEOBNRV4, a model for nonprecessing binaries [41]; SEOBNRV4_ROM, a fast surrogate model for SEOBNRV4 [41]; and SEOBNRV3, a model for precessing binaries [24, 40].

The IMRPHENOMPv2 model is a part of an approach that attempts to approximate the leading-order gravitational wave radiation using phenomenological fits to the Fourier transform of this radiation, computed from numerical relativity simulations and post-newtonian calculation [26, 42, 43]. Also using information about the final BH state, this phenomenological frequency-domain approach matches standard approximations for the post-Newtonian gravitational wave phase to an approximate, theoretically-motivated spectrum characterizing merger and ringdown. For IMRPHENOMPv2, precession is also incorporated by a “co-rotating frame” ansatz, here implemented via a stationary-phase approximation to the time-domain rotation operations performed for SEOBNRV3.

Surrogate models provide efficient and accurate representations of the gravitational wave strain, by interpolating between evaluations of a costly reference model. They have been applied to long duration signals [44, 45], arbitrarily many harmonic modes [27, 44], spinning binary systems [45, 46], and neutron star models with tidal effects [46]. In this work, we use surrogates developed to reproduce multimodal radiation from precessing binary systems [28, 29, 47]. These surrogates are demonstrably much more accurate in their domain of validity than the approximations described above. However, due to the limited duration and parameter space coverage, the surrogate we use here (NRSur7dq2,[29]) has a limited range of validity, to high masses; to mass ratios $m_1/m_2 < 2$; and to spins $|\chi_i| < 0.8$.

Models for binary neutron stars account for the response of each neutron star’s structure into their estimate for dynamics of and radiation from merger. Using frequency domain methods which generalize classic post-Newtonian calculations [48, 49], Dietrich et al [50] introduced a simple way to add leading-order tidal effects to the nonprecessing models described above. Recently Dietrich et al [51] implemented this effect into SEOBNRV4_ROM and IMRPHENOMD, which we denote by the postfix `_NRTIDAL`. These `_NRTIDAL` approximations were developed and calibrated using an effective one body model (TEOBRESUMS) that incorporates the effects of adiabatic tides and spin [52, 53]; see [51] and references therein. Another model (SEOBNRV4T) approximates binary inspiral and neutron star dynamics by allowing neutron stars to have both spin and dynamical tides

¹ This choice of merger phase behavior is known to be inconsistent with precessional dynamics during merger [29, 38].

[41, 54–56]. As described in part in [51], these approximations include tidal effects at differing levels of completeness. For example, among the models described here only TEOBRESUMS and SEOBNRV4T incorporate the quadrupole-monopole interaction [57] into the dynamics; only TEOBRESUMS includes higher modes into the outgoing radiation; and only SEOBNRV4T uses dynamic tides. While none of these models can account for neutron star spins that are misaligned from the orbital angular momentum, these models capture the leading-order features most relevant for small NS spins.

For most models, we employ `lalsimulation` implementations of these two approximations, provided and maintained by their authors in the same form as used in LIGO’s O1 and O2 investigations. For NR surrogate waveforms, we employ the software provided by the authors [58]. We use the implementation of TEOBResumS provided by the authors [59], restricting to $\ell = 2$ modes for the outgoing radiation.

Rather than rely on one of these diverse approximations for our synthetic fiducial sources, we instead almost always use the output of detailed simulations of Einstein’s equations, provided by the RIT and SXS group [60–62]. Table I provides the properties of our synthetic sources. All of the synthetic sources have parameters qualitatively consistent with the observed binary black hole population.

IV. VALIDATION EXAMPLES

In this section, we use both LI and RIFT to infer the parameters of three synthetic sources provided in Table I, using the models described in Section III. First and foremost, we use these examples to demonstrate both LI and RIFT produce equivalent results when used to analyze the same synthetic data with the same underlying model. To compactly characterize both the analysis method and model, we will use a prefix of LI or RIFT and a postfix of the model name; for example, a LI-SEOBNRV4_ROM analysis was performed with LI using the nonprecessing model SEOBNRV4_ROM. We also use these examples as an opportunity to further demonstrate how systematic differences between models can produce moderately different conclusions about each binary’s properties. In that context, we emphasize the contrast with other models and NRSur7dq2, which contains higher modes.

Each of the synthetic sources used in this work are created with the “zero noise realization”, such that the synthetic detector data is exactly equal to the expected response due to our synthetic source. For our binary black hole investigations, we assume gaussian detector noise in a two-detector, characterized by the same noise strain power spectrum adopted in our analysis of GW150914 in this and prior work [11]. Four our binary neutron star investigation, we assume gaussian noise in a three-detector network (Hanford/Livingston/Virgo) operating at design sensitivity. Each source has been scaled to have an SNR ~ 20 .

A. Aligned NR Source

The first synthetic source corresponds to the first row of Table I (RIT-1): an equal-mass binary black hole with $\chi_{1,z} = \chi_{2,z} = -1/4$ and $M = 80M_{\odot}$. For this analysis, we assume both spins are parallel to the orbital angular momentum, and adopt a uniform prior distribution in $\chi_{i,z}$ from the maximum to minimum allowed by each approximation. Using RIFT, we estimate the parameters with the following nonprecessing models: SEOBNRV4_ROM, IMRPHENOMD, and NRSur7dq2 with the latter using modes with $\ell \leq 3$. Using LI, we estimate the parameters with the same two former models SEOBNRV4_ROM and IMRPHENOMD. Figure 1 shows our inferred 90% credible intervals for several parameters for each of these algorithms and models, as well as associated one-dimensional marginal posterior distributions.

First and foremost, Figure 1 demonstrates that LI and RIFT produce comparable results when analyzing this data with SEOBNRV4_ROM (LI is dotted black, RIFT is solid black) as well as with IMRPHENOMD (LI is dotted blue, RIFT is solid blue). Second, due to the well-known good agreement between the nonprecessing models SEOBNRV4_ROM and IMRPHENOMD for the (2,2) mode [41, 64], we find very consistent posterior distributions for SEOBNRV4_ROM (black) and IMRPHENOMD (blue). Finally and also as expected, because these two models omit higher-order modes, an analysis with an NR surrogate model which includes several higher-order modes (here, $\ell_{max} = 3$) draws sharper conclusions about at least one of the parameters: the binary mass ratio. [Conclusions about the other parameters are not significantly impacted by including higher-order modes.] A similar result was found with a reanalysis of GW150914 where the LVC compared the data directly to NR [11].

B. Precessing NR Source

To test our approach on a precessing source, we generated a synthetic precessing signal using the second row of Table I (SXS-1), corresponding to a comparable-mass system with modest spins perpendicular to the orbital plane. We adopt a volumetric prior on each BH’s spin; see Appendix A 2. Using RIFT, we again estimate the parameters but this time with the fully precessing time-domain SEOBNRV3 and NRSur7dq2 models. Using LI, we infer source properties with the precessing frequency-domain IMRPHENOMPv2 model. Figures 2 show our inferred 90% confidence interval for each model, again with LI represented with dotted lines; RIFT results with solid lines; SEOBNRV3 in black; and IMRP in blue.

As expected, due to well-known differences between IMRPHENOMPv2 and SEOBNRV3, for example as demonstrated in [65], the conclusions derived using these two models do not perfectly agree.

ID	Model/Numerical Relativity	q	$M (M_{\odot})$	χ_{1x}	χ_{1y}	χ_{1z}	χ_{2x}	χ_{2y}	χ_{2z}	λ_1	λ_2
RIT-1	RIT:D12_q1.00_a-0.25_-0.25_n100	1.00	80.0	0.0	0.0	-0.250	0.0	0.0	-0.250	-	-
SXS-1	SXS:BBH:0308	1.23	110.0	0.117	0.0	0.320	0.335	0.0	-0.580	-	-
RIT-2	RIT:De10.D10.97_q1.3333_a-0.6_-0.8_n100	1.33	80.0	0.0	0.0	-0.600	0.0	0.0	-0.800	-	-
Tides-1	SEOBNRv4T	1.11	2.88	0.0	0.0	0.0	0.0	0.0	0.0	207	409

TABLE I: **Parameters of synthetic sources:** This table shows the parameters of all the synthetic sources (waveform approximant models and numerical relativity) used in this paper. q is the mass ratio defined with $q > 1$ (see Eq. 1), M is the detector-frame total mass, and χ_* are the components of the normalized spins (see Eq. 3). All luminosity distances are set such that the signal-to-noise ratio is around 20 (SNR \sim 20). Other extrinsic parameters are the following: inclination angle from the line-of-sight is $\iota = \pi/4$, right ascension is RA=0.57, declination is DEC=0.1, and the polarization angle is $\psi = \pi/4$

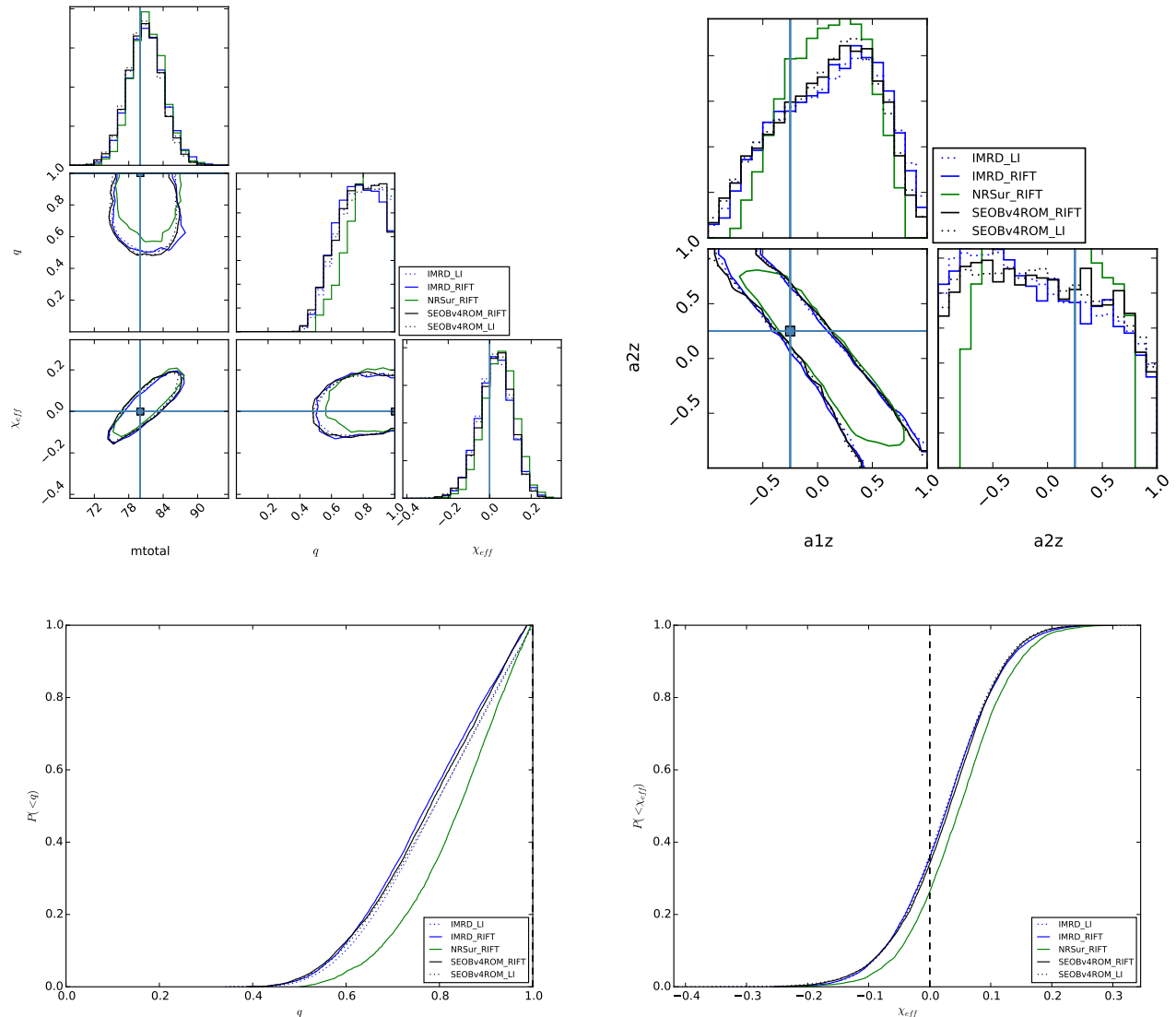


FIG. 1: **Recovery of nonprecessing NR source with nonprecessing analyses.** This figure shows inferred posterior parameter distributions for source #1 in Table I, generated using the CORNER package [63]. The top-left panel shows the one- and two-dimensional marginal distributions for M , q , χ_{eff} ; the top-right panel shows the one- and two-dimensional marginal distributions for $\chi_{1,z}$, $\chi_{2,z}$. The bottom two panels show the cumulative distributions of parameters q and χ_{eff} . In the two-dimensional plots, dotted contours are the 90% confidence intervals for the LI results using the IMRPHENOMD and SEOBNRv4_ROM models, while the three solid curves show RIFT results produced with IMRPHENOMD (blue, solid), SEOBNRv4_ROM (black, solid) and NRSur7dq2, restricted to aligned spins and including all modes up to $\ell = 3$ (green, solid). Both LI and RIFT produce comparable results when using IMRPHENOMD or SEOBNRv4_ROM, with statistical differences far smaller than model systematic effects (illustrated here with NRSur7dq2).

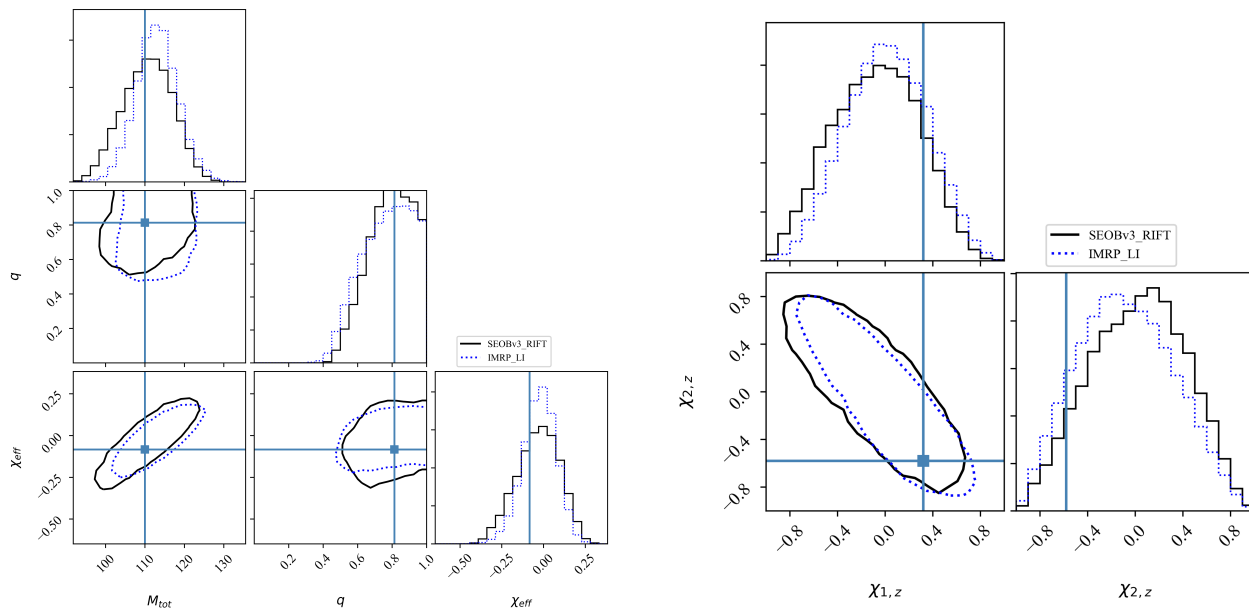


FIG. 2: **Recovery of a precessing NR source with a precessing model.** This figure shows the results using source #2 in Table I. The first group of plots shows the PE results in the total mass (M_{tot})-effective spin (χ_{eff})-mass ratio (q) parameter space (see Eq. 2 and Eq. 1 respectively). The second group of plots shows inferences about the two spin components $\chi_{i,z}$, where the z axis convention is defined as parallel to the orbital angular momentum.

C. Binary neutron star

Due to their low mass, binary neutron stars produce exceptionally long inspirals in the sensitive band of LIGO and Virgo. RIFT can not only efficiently analyze these signals, but do so while using exceptionally costly source models like SEOBv4T and TEOBResumS, which can require up to an hour to generate per source. As a concrete example, Figure 3 presents an analysis of synthetic data based on the Tidal-1 entry in Table I. Firstly, the dotted and solid blue contours and distributions show 90% credible intervals and one- and two-dimensional marginal distributions inferred from with LI and RIFT, both using the IMRPHENOMD waveform model, modified to include tides [51]. Both are consistent. Secondly, RIFT analyzed the data with the computationally expensive waveform models: SEOBv4T in red and TEOBResumS in orange. These again agree nicely with the previously mentioned IMRPHENOMD_NRTIDAL results as well as the LI-TaylorF2 in green. Using RIFT, we can not only recover the correct posterior, but we can do so with more costly waveforms when analyzing a binary neutron star system.

V. APPLICATIONS

A. Parameter inference via mixed models

Many approximations are well-suited only to certain parts of the parameter space, breaking down for sufficiently extreme spins, mass ratio, or total mass. For example, NRSur7dq2 is

only suitable for mass ratios $q > 0.5$ and $|\chi_i| < 0.8$. RIFT provides an almost-trivial mechanism to flexibly explore parameter inferences that employ different approximations A, B in different regions. Because the computational cost is dominated by ILE, once parameter inference is performed using models A and B separately, we can reanalyze the data with different mixtures of A and B with no additional overhead. For simplicity and to illustrate the method, we will employ the most extreme and simple form of this approach, where the training pairs $(\lambda_k, \ln \mathcal{L}_{\text{marg}}(\lambda)_k)$ used to produce a fit for $\ln \mathcal{L}_{\text{marg}}(\lambda)$ are provided using model A when λ_k is in some region \mathcal{V} , but with model B everywhere outside \mathcal{V} .

As a concrete and practical motivation for this strategy, Figures 1 and 5 show analysis of synthetic NR sources with IMRPHENOMD and with NRSur7dq2, assuming a nonprecessing binary and adopting a uniform- $\chi_{i,z}$ prior on the two BH spins. The hard limits on NRSur7dq2 both in mass ratio and particularly in $\chi_{i,z}$ have a substantial impact on our conclusions about spins and, for systems with large $|\chi_{\text{eff}}|$, even about χ_{eff} and hence about other parameters of the binary. Because constraints on χ_{eff} strongly correlate with information extracted about binary masses, this limitation is not academic, and can complicate attempts to apply these kinds of limited-support waveforms to probe effects like waveform systematics.

Figure 4 shows an analysis of the same source (RIT-2) as Figure 5, using RIFT with a hybrid analysis that uses NRSur7dq2 with $\ell \leq 2$ modes in its domain of validity, and IMRPHENOMD elsewhere. As demonstrated by Figure 5, restricting parameter inference to the domain of validity of NRSur7dq2 has a significant impact on the inferred source

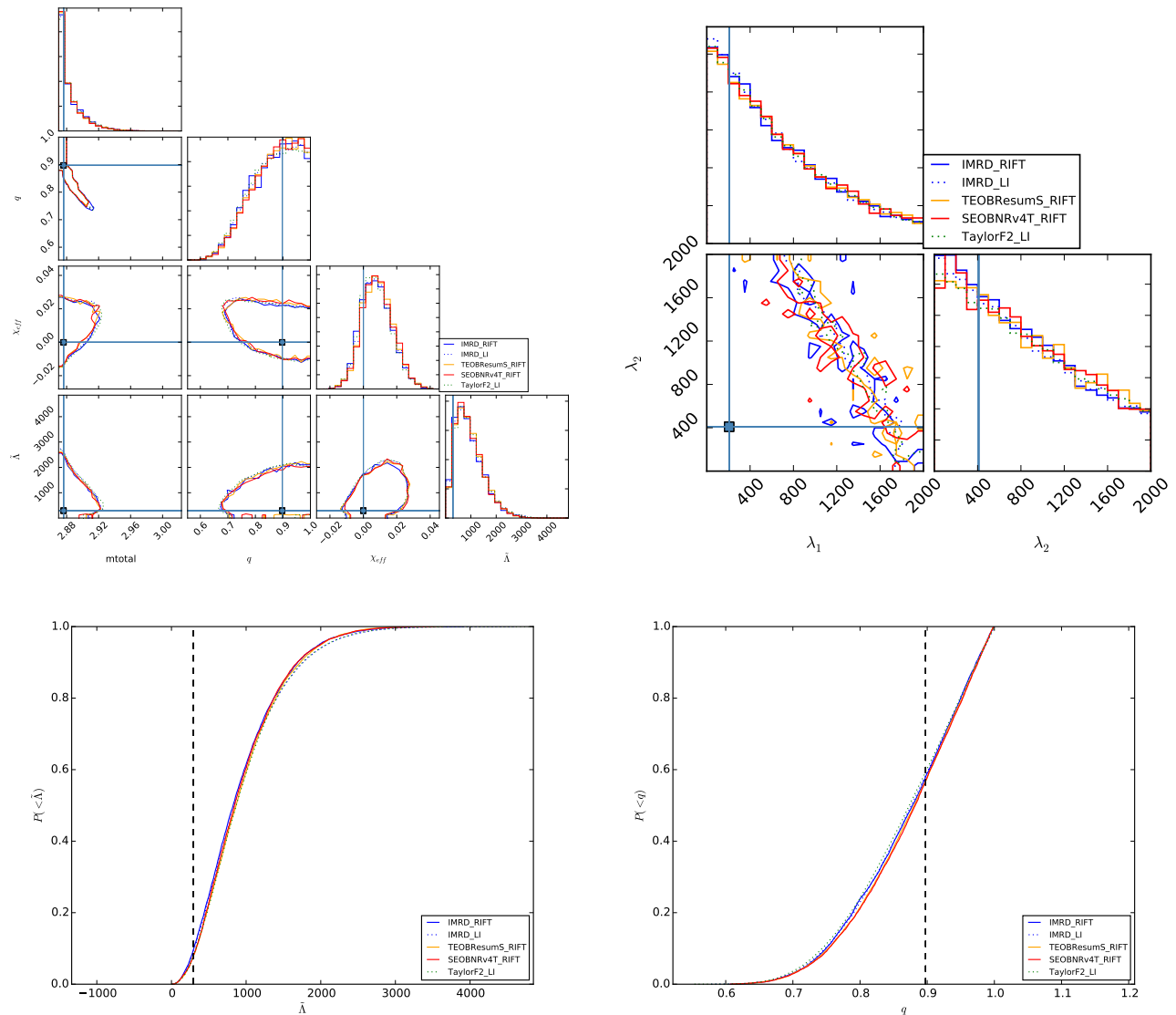


FIG. 3: Using sophisticated tidal waveforms to analyze tidal injections This figure shows inferences about the Tidal-1 source Table I, performed adopting the spin prior in Eq. (A7) with $\chi_{\max} = 0.05$. As in previous figures, the one- and two-dimensional results show all possible one-dimensional posterior distributions and two-dimensional 90% credible intervals for the total mass (M), mass ratio (q), effective tidal deformability ($\tilde{\Lambda}$), and net effective spin (χ_{eff}). As previously, dotted contours and curves correspond to LI results; solid curves are produced with RIFT; and different colors correspond to different waveform models: TaylorF2 is green, IMRPHENOMD_NRTIDAL is blue, SEOBNRv4T is red, and TEOBResumS is orange.

parameters. By contrast, the mixed model result agrees with inferences adopted with IMRPHENOMD. For the purposes of illustration we have intentionally selected a source both where the domain of validity of NRSur7dq2 impacts multiple astrophysical inferences and where extending the model produces comparable results. However, as also illustrated with Figure 5, even in this extremely astrophysically pertinent example, these mixed models are being applied in a regime where IMRPHENOMD and SEOBNRv4_ROM disagree. In a subsequent investigation, we will follow up this proof-of-concept example with a more detailed analysis of the advantages and applications of this mixed-model strategy, particularly for as-

sessing waveform systematics.

B. Investigating systematics

The method provides a particularly straightforward but deep method to assess the impact of systematics on posterior distributions. Simply put, if A and B are two models, we can use precisely the same evaluation points λ_α to estimate the marginalized likelihoods according to both models ($\ln \mathcal{L}_\alpha(A)$ and $\ln \mathcal{L}_{\text{marg}\alpha}(B)$), and hence to estimate the corresponding posterior distributions. In practice, we first generate a poste-

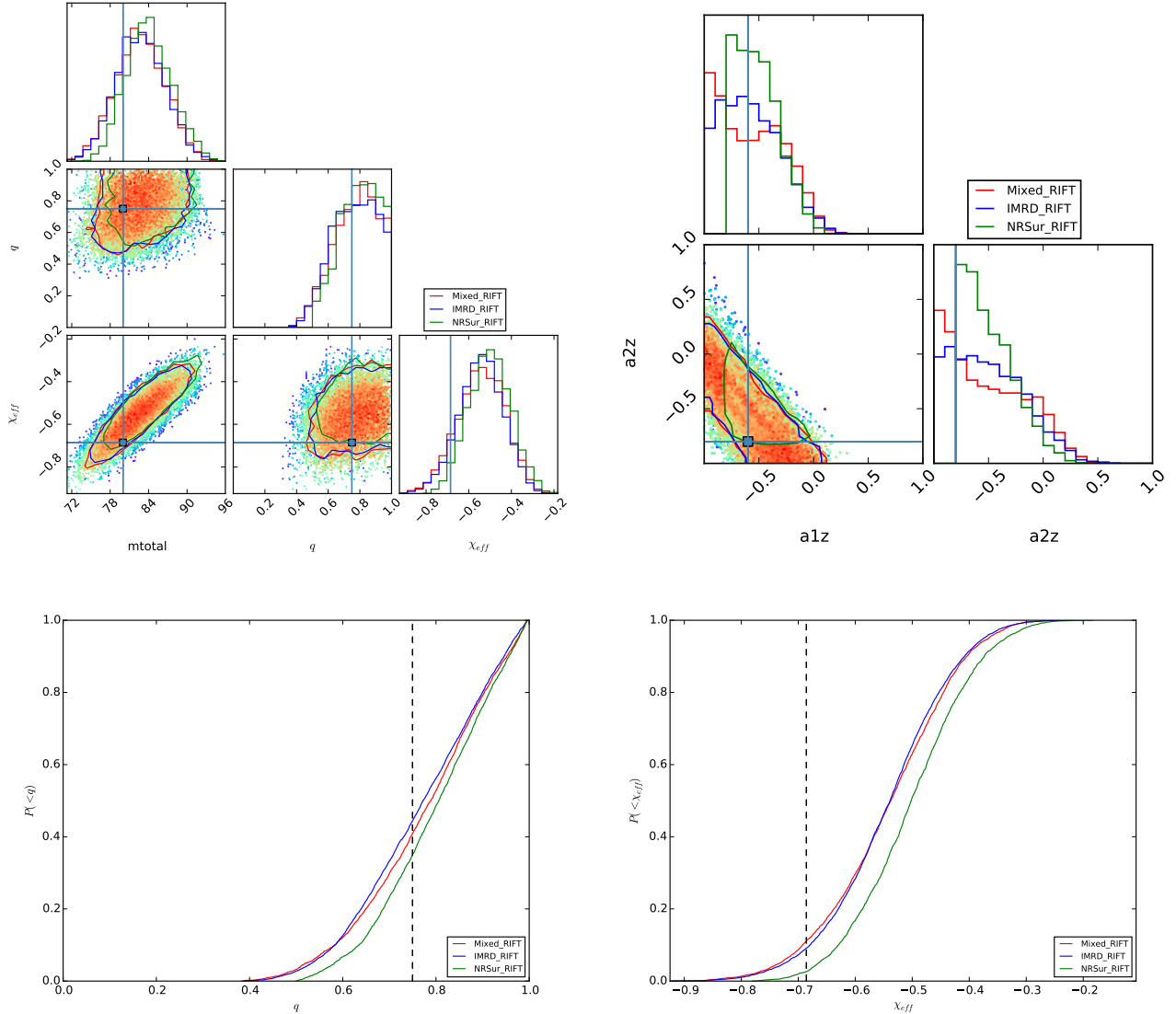


FIG. 4: **Mixing models for a single analysis** This figure shows the inferred parameters for source RIT-2, in a format similar to Figure 1. The colored curves represent 90% credible intervals derived only using IMRPHENOMD (blue), NRSur7dq2 with $\ell = 2$ modes only (green), or using a mixture of models (red). In the mixture approach, we employ NRSur7dq2 with modes up to $\ell_{\max} = 2$ in its region of validity ($1/q > 0.5$ and $a_i < 0.8$) and IMRPHENOMD elsewhere.

rior distribution using the iterative procedure described above for model A (e.g., SEOBNRv4) and then, using all the test points proposed during the iterative scheme, derive the corresponding posterior for model B . This approach provides not only the posterior distributions but also the ingredients needed for a detailed investigation into the origin of any discrepancies: the point-by-point differences between $\ln \mathcal{L}_{\text{marg}\alpha}(A)$ and $\ln \mathcal{L}_{\text{marg}\alpha}(B)$, as a function of model parameters. Once differences are identified, the ability to quickly produce a single scalar diagnostic for model differences ($\ln \mathcal{L}_{\text{marg}}$) enables detailed and easily-understood diagnostics as users change one feature of their calculation at a time (e.g., mode content; data conditioning or noise model).

Figure 5 shows a concrete illustration of this strategy,

applied when interpreting the nonprecessing binary source model RIT-2. In this case, parameter inference was performed using a fiducial model to generate a sequence of ever-finer evaluation grids. The net grid was then applied to two other models, leading to different predictions. Because these models all rely on the same input grid λ_α , we can directly diagnose which features drive differences in our posterior distributions. For example, in this case (Figure 5) this strategy helps us assess the relative role of restricted χ_i versus model differences such as higher modes in changing inferences about χ_{eff} and hence M, q .

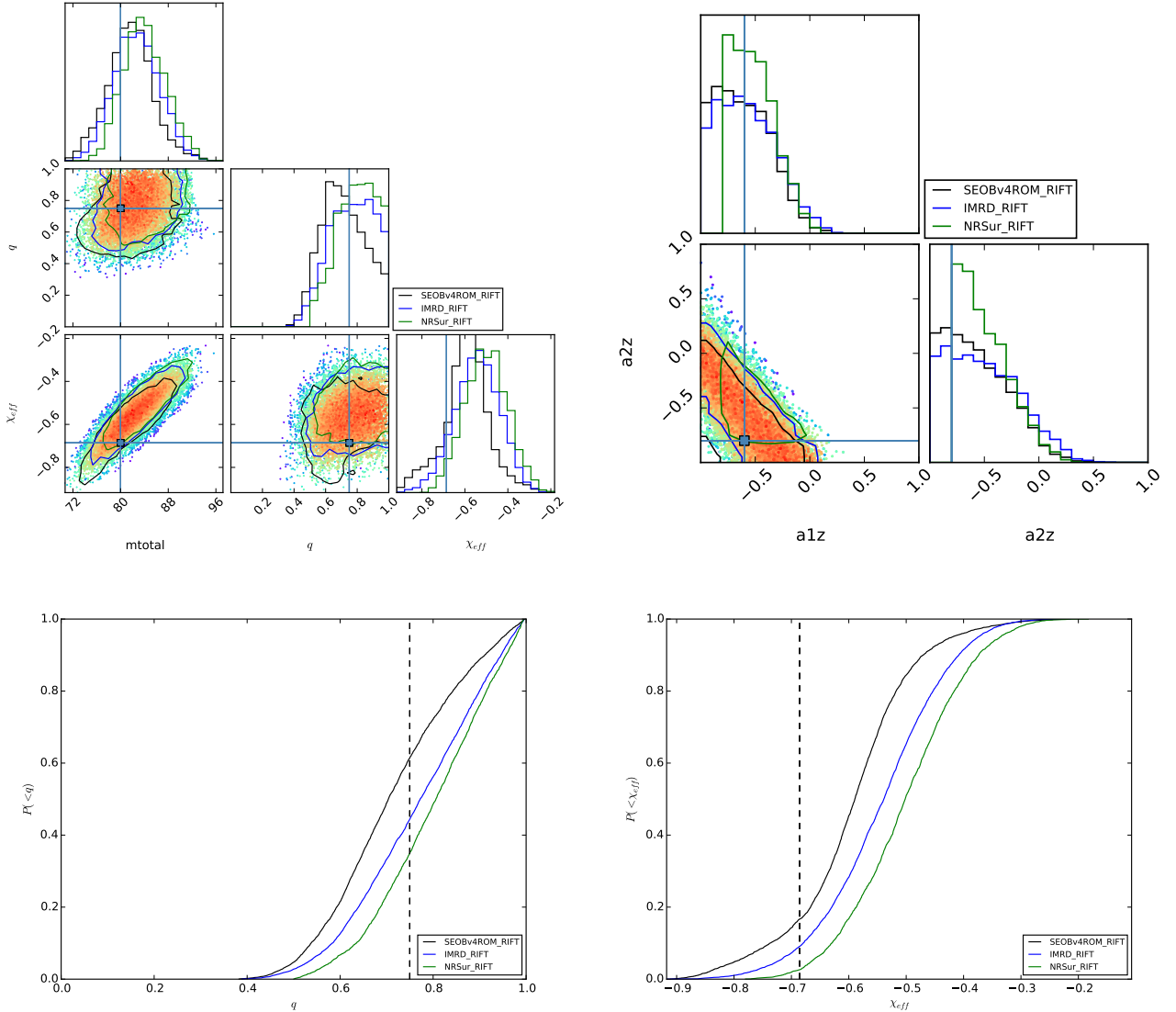


FIG. 5: **Different models on the same parameter grid** This figure shows inferences about RIT-2, described in Table I. The contours, points, and curves used in this figure are styled according to scheme described in Figure 1. Points are colored using likelihood values obtained from SEOBv4ROM.

C. Astrophysical population inference

Since RIFT separates the process of estimating the likelihood and producing fair draws from the posterior, it is ideally suited for astrophysical inference, where all events are reassessed concurrently with different astrophysical priors. In this application, the ability to robustly explore alternative priors is paramount, particularly when future observations may motivate detailed reanalysis of earlier events. As described in Section II and Appendix A, RIFT can efficiently generate posterior distributions using any prior whatsoever, by performing a suitable Monte Carlo.

In principle, other methods can also reanalyze existing re-

sults using alternative priors. Notably, with a sufficiently large list of posterior samples performed using a prior without compact support, the procedures described in Section II could produce weighted samples suitable to any prior. However, as emphatically demonstrated by all of our figures (Figs 2) and by Williamson et al [65], a finite list of samples from our posterior distribution with fiducial priors have compact support. For precessing binaries, previous analyses do not sample extremal spin. By contrast, by preserving the full (marginalized) likelihood, RIFT can evaluate the implications of a nearly arbitrarily extreme choice of prior, with minimal additional computational cost. In related work [66], we employ this approach with RIFT inputs for astrophysical inference.

D. Inferences about the nuclear equation of state

RIFT provides direct estimates of the (marginalized) likelihood $\ln \mathcal{L}_{\text{marg}}(\boldsymbol{\lambda})$, allowing us to carry out subsequent calculations which require it. As a concrete example, we can more efficiently deduce the nuclear equation of state by post-processing generic calculations performed by RIFT without added computational expense.

Specifically, in Section IV C and Figure 3 we carried out model-independent inference of binary neutron star masses, spins, and tidal deformabilities λ . Any proposed nuclear equation of state imposes a specific relationship between the (source-frame) neutron star gravitational masses m_i and the tidal λ parameter ($\lambda(m_i) = \lambda_i$). Imposing this relationship, we can repeat our parameter inference both to draw tighter inferences about binary parameters and to deduce how well the proposed equation of state matches the data, after marginalizing over all other quantities. With RIFT, this reanalysis requires a particularly efficient re-use of the marginalized likelihood $\ln \mathcal{L}_{\text{marg}}(m_{1,z}, m_{2,z}, \lambda_1, \lambda_2, \chi_1, \chi_2)$ as a function of its parameters: the redshifted detector-frame masses $m_i(1+z) = m_{i,z}$; the two neutron star tidal deformabilities λ_i ; and the two neutron star spins $\chi_i \in [-\chi_{\text{max}}, \chi_{\text{max}}]$, assumed parallel to the orbital angular momentum. Specifically, for each proposed equation of state, characterized by some hyper-parameters γ , we evaluate the a quantity equivalent to the evidence $\int d\boldsymbol{\lambda} \mathcal{L}_{\text{marg}}(\boldsymbol{\lambda}) p(\boldsymbol{\lambda})$ appearing in Eq. (8):

$$I(\gamma) = \int dm_1 dm_2 d\chi_1 d\chi_2 p(\chi_1, \chi_2) dz p(z|m_1, m_2) \mathcal{L}_{\text{marg}}(m_1(1+z), m_2(1+z), \lambda_1(m_1|\gamma), \lambda_2(m_2|\gamma), \chi_1, \chi_2) \quad (11)$$

where $p(z)$ is the posterior redshift distribution given a source with masses m_1, m_2 was observed, which can be efficiently extracted from RIFT or tightly constrained by electromagnetic observations. Appendix C describes techniques to efficiently evaluate this expression for generic observations. Just as with $\mathcal{L}_{\text{marg}}$ and intrinsic binary parameters, we can evaluate the marginalized likelihood $I(\gamma)$ on a grid of equation of state parameters; interpolate; and generate posterior distributions over those equation of state parameters, for one or more events.

Figure 6 shows a concrete example of this procedure, applied to the spectral equation of state parameterization introduced by Lindblom [67, 68] and to a synthetic BNS generated using the APR4 equation of state [69], as previously analyzed in Figure 3. For this low-redshift source, similar to GW170817, we will assume the redshift is well-determined, eliminating that factor in the integrand. [Equivalently, for this low-redshift source, the source-frame and detector-frame masses are sufficiently similar that $\lambda(m_{1,z}|\gamma) \simeq \lambda(m_1|\gamma)$ (i.e., the data can't discriminate between them) so the integral over redshift can be performed once and for all, and all remaining expressions carried out using redshifted masses; see Appendix C.] As a concrete proof of concept, this figure shows the marginalized likelihood derived from this single event as a function of two spectral equation of state parameters, as well as Bayesian inferences about those two equation of state parameters when holding others fixed. In this analysis, we include only causal equations of state ($v < c$) and require a maximum neutron star mass greater than $2M_\odot$, motivated by measurements of PSRs 1614-2230 and J0348+0432 [70, 71]. More generally, other observational and theoretical constraints will provide a prior $p(\gamma)$ on the equation of state parameters. In terms of this prior, the marginal posterior distribution on equation of state parameters is proportional to $I(\gamma)p(\gamma)$, and the marginal posterior distribution for any other expression of interest follows by either quadrature or use of weighted samples, as before. As a concrete example, if γ_α are n representative EOS configurations from the marginal posterior distribution and, for each α , we generate a Monte Carlo approximation to Eq. (11) and retain the weighted samples $(w_{k,\alpha}, \boldsymbol{\lambda}_{k,\alpha})$ for $k = 1 \dots N$ needed to evaluate it, then the marginal distribution of $\tilde{\Lambda}$ [Eq. (A18)] follows by Monte Carlo integration of the cumulative distribution:

$$P(< \tilde{\Lambda}) \simeq (nN)^{-1} \sum_{k,\alpha} w_{k,\alpha} p(\gamma_k) \Theta(\tilde{\Lambda} - \tilde{\Lambda}(\boldsymbol{\lambda}_{k,\alpha})).$$

By providing marginalized likelihoods $I(\gamma)$, this approach to EOS inference enables the same powerful embarrassingly-parallel and postprocessing-dominated approach used by RIFT itself. For example, we can combine inferences from multiple events by simply multiplying the associated likelihood distributions [$I(\gamma|d_1)I(\gamma|d_2) \dots$]. The end-user is free to efficiently adopt any prior of interest after the initial analysis; to assess whether choice of priors limits or dominates their analysis; and to incrementally extend their parameter space exploration with the minimum necessary computational expense. This approach is well-suited to rapidly-converging and low-dimensional parameterizations like the spectral method shown in Figure 6. However, due to the remarkably low cost of all integrals involved and our reliance on precomputed marginalized likelihoods, this approach can also be applied to assess generic EOS parameterizations inside standard Markov chain Monte Carlo algorithms. Though the above discussion is written as if equation of state dependence enters only through the tidal deformabilities λ , this procedure works when the underlying dynamics and radiation models include additional multipolar couplings. While similar parameterized equations of state have already been developed and used to infer the equation of state from individual BNS GW measurements [72], our approach will make the best use of multiple observations, as we don't need additional infrastructure or approximations to estimate $I(\gamma)$.

For low-redshift sources like GW170817 where $\lambda(m_z) \simeq \lambda(m)$ and hence where the redshift distribution $p(z|m_1, m_2)$ is not needed, and equivalently for sources with known host galaxy redshifts, we have also explored an alternative approach to compute $I(\gamma)$. In this approach, we evaluate $\ln \mathcal{L}_{\text{marg}}$ on a grid of mass and spin choices, using the spec-

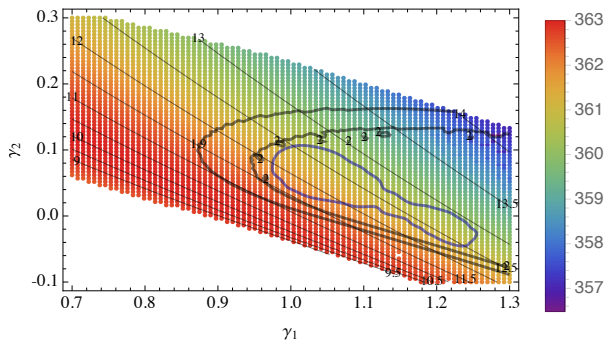


FIG. 6: **Inferences about the equation of state:** Colors indicate the marginalized likelihood $I(\gamma)$ versus the two parameters γ_1, γ_2 of the Lindblom et al spectral EOS representation, applied to a binary neutron star source similar to Tidal-1. For context, the thin gray lines show contours of constant radius of a $1.5 M_\odot$ neutron star, according to this equation of state [$R(m = 1.5 M_\odot)$]; the two heavy black lines show contours of constant maximum mass for $2M_\odot$ and $1.9M_\odot$, respectively. For the purposes of this proof-of-concept calculation, we explore only these two variables, fixing the remaining spectral EOS parameters to $\gamma_3 = \gamma_4 = 0$, $p_o = 2.272 \times 10^{33}$ dyne/cm², $x_{max} = 7.25$, and $\epsilon_o/c^2 = 2.05 \times 10^{14}$ g/cm³. The solid blue line shows the 90% credible interval on the inferred equation of state, after restricting to a causal EOS and restricting the maximum mass to be greater than $1.97M_\odot$.

ified EOS to determine $\lambda_i = \lambda(m_i|\gamma)$. We then perform the usual RIFT approach to estimate $\ln \mathcal{L}_{\text{marg}}$ and hence to compute $\int d\lambda \mathcal{L}_{\text{marg}}(\lambda) p(\lambda)$, a byproduct of the Monte Carlo integration procedures used to generate our posterior distributions. While this approach can be useful for ranking the relative validity of a few EOS, its duplicative computations and omission of redshift make it too burdensome for long-term use.

VI. ANALYSIS OF REAL EVENTS

In this section, we demonstrate our method can reproduce the interpretation of LIGO coalescing binary black holes. Though we do not not always include head-to-head examples with the same approximations, these examples demonstrate our code functions well even on real LIGO detector noise. These examples also demonstrate that a feature omitted from RIFT but included in LI – marginalization over uncertain detector calibration – has no impact on our estimates of intrinsic source parameters. Gravitational wave strain data identical to the inputs employed here are available from the LIGO Open Science Center [73].

A. Reproducing the interpretation of a real GW source: GW150914

In this section, we analyze GW150914 with RIFT and LI using several different approximate waveform models. In these comparisons, we employ real LIGO data to analyze

GW150914, estimating strain noise power spectral densities (PSDs) for both events from data segments near each event, similar to the PSDs used in [4]. We also employ different spin priors, such as the volumetric spin prior [Eq. (A4)], than those employed by Abbott et al. [3, 74] in the original analysis of this event. Our analysis also differs from these previously-published results insofar as we do not marginalize over the calibration uncertainty of the data. The effect of calibration uncertainty on the intrinsic parameter posterior distribution is small. Finally, to be consistent with previous analyses with numerical relativity simulations [11] and keeping in mind finite model duration, when using NRSur7dq2 we adopt a minimum frequency of 30Hz; however, we adopt a minimum frequency of 20Hz for our other analyses. The choice of lower cutoff frequency has little impact on our comparisons [11].

Figure 7 shows our analyses of GW150914 with LI and RIFT using nonprecessing waveform models, all computed using a prior where that each $\chi_{i,z}$ is a uniform random number. First and foremost, the good agreement between the solid and dotted blue lines (IMRPHENOMD) demonstrates how LI and RIFT agree when applied to the same data with the same noise model, even in real detector noise. Second, as in previous result derived by directly comparing GW150914 to numerical solutions of Einstein’s equations [11], we find that our posterior inferences derived a waveform model that includes higher modes (here, NRSur7dq2 with $\ell \leq 3$) more sharply constrains some parameters like the binary mass ratio q . Additionally, as we adopt a more flexible likelihood model, we may also better constrain several other parameters relative to the analysis presented in NRSur7dq2. However, our analysis and previous results [11] suggest that, in an aligned-spin analysis of this event which adopts a prior not strongly disfavoring anti-aligned spins, the posterior has substantial support outside of the domain of validity of NRSur7dq2. As demonstrated previously in Figure 4, the domain of validity of NRSur7dq2 can impact inferences, if the posterior support extends to the edge of the model domain. In a companion study devoted to direct comparison to numerical relativity solutions, we will more carefully address differences between this result and the analysis presented in [11], using numerical relativity simulations to fill the gaps.

Next, to provide a comparison that allows for all spin degrees of freedom, we analyze with GW150914 RIFT and SEOBNRV3 [75] or NRSur7dq2 ($\ell \leq 3$), on the one hand, and with LI and IMRPHENOMPV2 [3, 4] on the other. Figure 8 shows the 90% confidence intervals for the RIFT+SEOBNRV3, RIFT+NRSur7dq2 ($\ell \leq 3$), and LI+IMRPHENOMPV2 analyses in black, green, and dotted blue, respectively. First and foremost, consistent with our and other prior work, we see differences between the posterior inferences derived using different waveform approximations and assumptions, even for sources like GW150914 with now-fiducial binary parameters and source amplitudes. Second, consistent with an earlier investigation of GW150914 which directly compared it to numerical relativity simulations [11], we see that including higher harmonics enables us to draw sharper conclusions about binary parameters – here, the binary mass ratio. Our analysis differs from that prior inves-

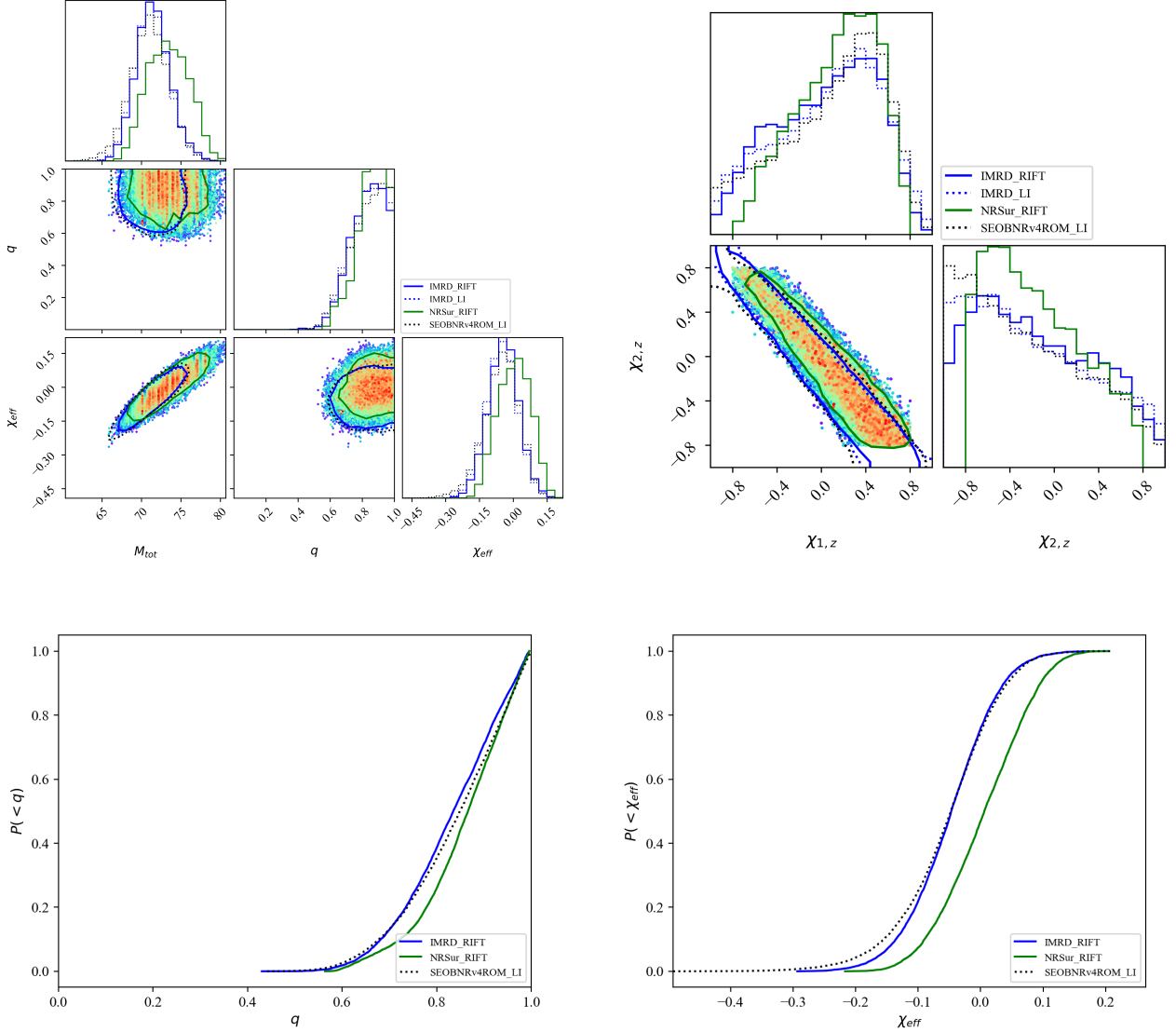


FIG. 7: **Reanalysis of GW150914: Aligned models** - This figure shows the results of a reanalysis of the first GW detection GW150914, using a prior where each $\chi_{i,z}$ is a uniform random number and the assumption that both spins must be parallel to the orbital angular momentum. The top two panels show one- and two-dimensional marginal distributions in redshifted total mass M_{tot} , q , χ_{eff} and in the components of each BH's spin ($\chi_{i,z}$) along the orbital angular momentum. The bottom panel provides one-dimensional marginal cumulative distributions for q and χ_{eff} , to highlight differences between different approaches. Curves are colored and styled following the convention adopted in previous figures; in particular, black lines correspond to SEOBNRV4_ROM, solid green lines to NRSur7dq2 with the spins restricted along the orbital angular momentum with all modes up to $\ell_{max} = 3$, and dotted blue lines to IMRPHENOMD. The top right and hence bottom left panels show significant differences between NRSur7dq2 and other approximations principally due to the range of validity of the NRSur7dq2 model, which is valid only for $1/q > 0.5$ and $|\chi_i| < 0.8$.

tigation work in two key ways: precessing inference and χ limits. While the previous study [11] compared GW150914 to generic simulations, a posterior distribution was estimated only on the basis of *nonprecessing* simulations; by contrast, our analysis employs a fully precessing model. Conversely, our use of NRSur7dq2 is limited to $|\chi_i| < 0.8$, which directly constrains our ability to draw generic inferences about BH spins.

B. Reanalysis of LVT151012

To demonstrate RIFT's ability to estimate nongaussian posteriors of low-significance events in real detector noise, Figure 9 presents parameter inferences for LVT151012 with RIFT and LI, performed with SEOBNRV3 (black) and IMRPHENOMPV2 (blue dotted) respectively. The analysis uses frequencies between $f_{min} = 20\text{Hz}$ and 1700Hz , with a volumetric spin prior. The two analyses demonstrate a level of agree-

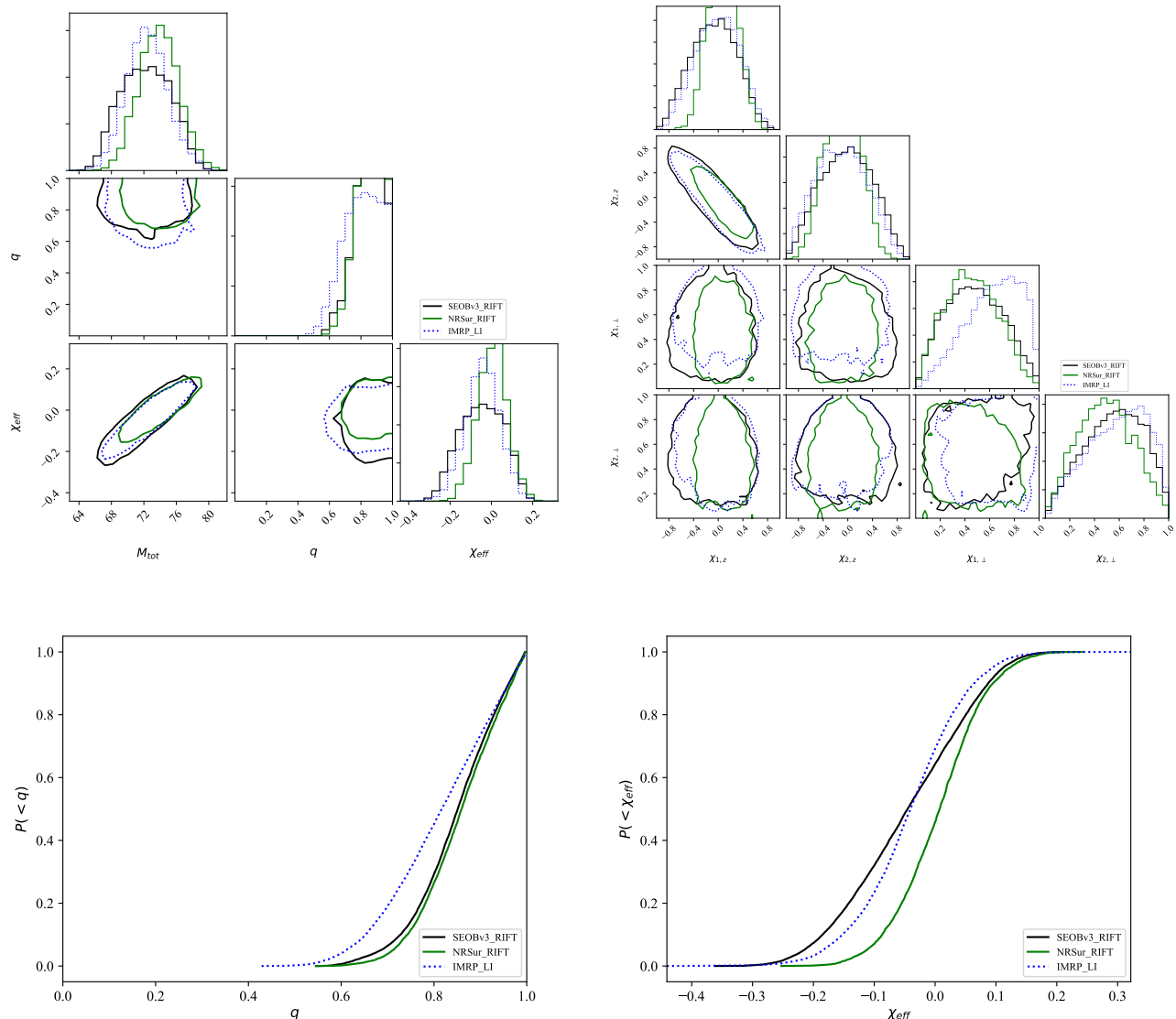


FIG. 8: **Reanalysis of GW150914: Precessing models** - This figure shows the results of a reanalysis of the first GW detection GW150914, using the volumetric spin prior [Eq. (A4)] and waveform models that allow for spin-orbit misalignment. The top two panels show one- and two-dimensional marginal distributions in redshifted total mass M_{tot} , q , χ_{eff} and in the components of each BH’s spin along $(\chi_{i,z})$ and perpendicular $(\chi_{i,\perp})$ to the orbital angular momentum. The bottom panel provides one-dimensional marginal cumulative distributions for q and χ_{eff} , to highlight differences between different approaches. Curves are colored and styled following the convention adopted in previous figures; in particular, black lines correspond to SEOBNRV3, solid green lines to NRSur7dq2 with fully precessing spins with all modes up to $\ell_{\text{max}} = 3$, and dotted blue lines to IMRPHENOMPV2. The top right panel shows significant differences between NRSur7dq2 and other approximations principally due to the range of validity of the NRSur7dq2 model, which is valid only for $1/q > 0.5$ and $|\chi_i| < 0.8$.

ment consistent with previously-demonstrated model systematics.

While we have also performed a corresponding analysis of LVT151012 with NRSur7dq2, including higher harmonics. Within the range of mass ratios accessible to NRSur7dq2, we see good agreement between an analysis with SEOBNRV4 and NRSur7dq2. However, due to the limited q domain of NRSur7dq2, we defer a detailed quantitative discussion of higher modes in LVT151012 to companion work employing numerical relativity simulations to fill the gaps.

VII. DISCUSSION

We have introduced and validated RIFT, a strategy to iteratively produce high-precision posterior distributions of binary parameters for a wide variety of candidate compact binary coalescences. We demonstrated by example how this method could employ costly and even heterogeneous approximations. As concrete illustrations of its utility, we have employed computationally taxing models, which require up to one hour per waveform evaluation, to infer parameters of synthetic binary

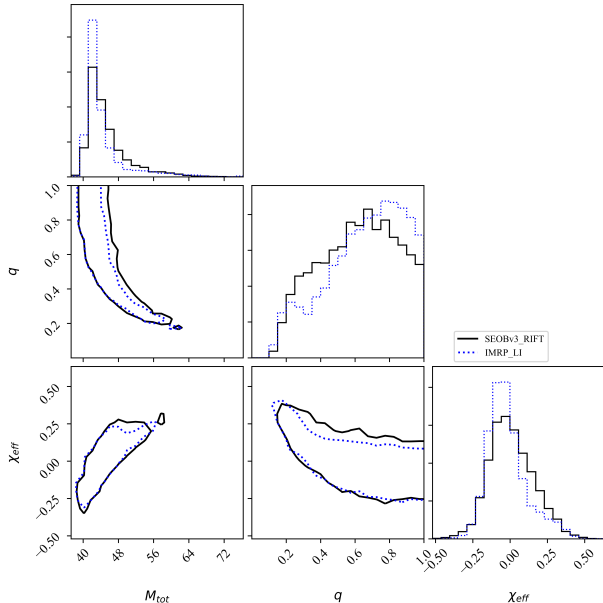


FIG. 9: **Reanalysis of LVT151012** This figure shows two analyses of LVT151012. The 2D plot shows the PE results in the effective spin (χ_{eff})-mass ratio (q) parameter space (see Eq. 2 and Eq. 1 respectively). The other two panels show the corresponding 1D distributions for each parameter. Curves and 90% contours have been colored and styled following the conventions of previous analyses.

neutron star systems; demonstrated this approach reproduces the results of other inference strategies, when employing the same approximations; and provided proof-of-concept demonstrations of new strategies to identify, assess, and remedy systematic errors which our method uniquely enables.

While RIFT does not have the very mature feature set provided by LI, including marginalization over calibration error, this approach is compatible with these extensions, and can exist simultaneously with other approaches within future parameter inference strategies for gravitational wave sources.

The tools demonstrated in this work are actively being generalized. For example, the gaussian process interpolation strategy can and has been trivially applied to the (fixed) grid provided by numerical relativity simulations, generalizing prior work [11, 76]. Described in a companion work [14], this approach was performed to supplement the analysis of GW170104, GW170608, and GW170814 [5–7]. Our strategy can also be trivially employed to construct posterior distributions that mix approximations, using different approaches in different parts of parameter space, with the boundaries differentiating between approximations chosen post-facto and with essentially negligible additional computational cost, besides post-processing.

While RIFT produced results with dramatically smaller wall-clock time, the investigations performed in this work had overall CPU costs comparable to or even in excess of a corresponding LI analysis with low-cost waveform models. In the future, when overall computational efficiency becomes a

more important constraint on our investigations, we will describe optimizations to this strategy which reduce our overall computational burden.

Acknowledgments

The authors thank Prayush Kumar, Juan Calderon-Bustillo, Chris Pankow, Les Wade, and Matt Carney for constructive discussions during this investigation, and Ben Farr for feedback on the draft. The authors particularly thank Sebastiano Bernuzzi and Alessandro Nagar for their assistance in interfacing with the latest version of TEOBResumS. ROS and JAL gratefully acknowledge NSF award PHY-1707965.MR gratefully acknowledges support from the RIT College of Science. The authors thank to the LIGO Scientific Collaboration for access to the data and gratefully acknowledge the support of the United States National Science Foundation (NSF) for the construction and operation of the LIGO Laboratory and Advanced LIGO as well as the Science and Technology Facilities Council (STFC) of the United Kingdom, and the Max-Planck-Society (MPS) for support of the construction of Advanced LIGO. Additional support for Advanced LIGO was provided by the Australian Research Council. Finally, the authors are grateful for computational resources used for the parameter estimation runs provided by Cardiff University in Cardiff, UK, funded by an STFC grant supporting UK Involvement in the Operation of Advanced LIGO; the Albert Einstein Institute at Hanover, Germany; and the LIGO Lab computing facilities at Caltech, Hanford, and Livingston, maintained by the California Institute of Technology at Pasadena, California.

Appendix A: Coordinate systems and priors

In this appendix, we summarize the coordinate systems and priors adopted to perform the fit and in particular carry out the Monte Carlo integration procedure for $\ln \mathcal{L}_{\text{marg}}$ which produces weighted posterior samples, as described in Section II. The design structure of the adaptive Monte Carlo integrator developed for ILE and re-used in our code drives several prior and coordinate choices. At a very low level, the adaptive procedure assumes the initial true prior p and (adapted) sampling prior p_s are both separable: $p(x_1 \dots x_n) = p(x_1)p(x_2) \dots p(x_n)$ for $\{x_1 \dots x_n\}$ the coordinate system used to perform the Monte Carlo. Moreover, because the adaptive procedure optimizes each sampling prior p_s in one coordinate at a time, the overall algorithm’s performance dramatically improves when the posterior is compatible with this coordinate system (i.e., the posterior approximately fills a sub-hypercube of our computational domain). Whenever we have confident reason to suspect a particular parameter does not impact the posterior distribution whatsoever, we can analytically marginalize over superfluous parameters and perform a fit which omits these parameters. Finally, we can explore alternative priors by using weighted posterior samples, using the ratio of new prior relative to reference prior in all coordinate dimensions.

1. Masses

We adopt a uniform prior over the (detector-frame) masses m_1, m_2 (with $m_1 \geq m_2$), which can be expressed in several equivalent coordinate systems by a suitable Jacobian transformation. Following past practice, we nominally employ a triangular region with $m_i \geq m_{min}$ and $M = m_1 + m_2 \leq M_{tot,max}$; the prior is $p(m_1, m_2) = 2/(M_{max} - m_{min})^2$, if both regions $m_1 > m_2$ and $m_1 < m_2$ are included in the integration, and twice that otherwise. In most cases, we perform our underlying calculations in \mathcal{M}, η coordinates, where $\mathcal{M} = (m_1 m_2)^{3/5}/(m_1 + m_2)^{1/5}$ and $\eta = m_1 m_2/(m_1 + m_2)^2$. In these coordinates, the prior can be represented as [10]

$$p(\mathcal{M}, \eta) = \frac{4}{(M_{max} - m_{min})^2} \frac{\mathcal{M}}{\eta^{6/5} \sqrt{1 - 4\eta}}. \quad (\text{A1})$$

As this prior diverges at $\eta = 1/4$, it is not well-suited to posterior distributions with significant support very close to the equal mass line, like binary neutron stars. For such cases, we change coordinates to $\delta = \sqrt{1 - 4\eta}$; the prior becomes

$$p(\mathcal{M}, \delta) = \frac{16 \times 2^{2/5}}{(M_{max} - m_{min})^2} \frac{\mathcal{M}}{(1 - \delta^2)^{6/5}}. \quad (\text{A2})$$

In rare cases, we may employ coordinates M and $q = m_2/m_1$; in this case, prior is [13]

$$p(M, q) = \frac{4}{(M_{max} - m_{min})^2} \frac{M}{(1 + q)^2}. \quad (\text{A3})$$

For confident detections, the mass posterior will not have significant support outside a compact region. Because we can freely change the prior in regions far outside the posterior and not impact results, we often adopt technically convenient boundaries. For example, rather than transform the triangular region of permissible masses m_1, m_2 to a more complicated boundary in \mathcal{M}, η , we simply adopt suitable intervals in M and η which contain the posterior.

2. Spins

The spin degrees of freedom are characterized by the spin angular momenta \mathbf{S}_i or equivalently their dimensionless spins χ_i/m_i^2 . For most astrophysically relevant scenarios, the posterior distribution strongly constrains χ_{eff} [Eq. (2)] but not the complementary combination of aligned spins. Lacking a compelling astrophysically-motivated choice, several spin-dependent priors have been adopted, which employ different numbers of spin degrees of freedom.

Volumetric spin prior (generic, cartesian): By default, we employ a prior which is uniform in each component of the dimensionless spins χ_i in some hypercube: $\chi_i \in [-\chi_{max}, \chi_{max}]$. After generating posterior samples, we then eliminate samples with either dimensionless spin above our threshold ($|\chi| > \chi_{max}$). Combined, our hypercube-plus-cut procedure produces an effective prior that is uniform over the volume of

a coordinate sphere of radius χ_{max} :

$$p_{vol}(\chi_i, \theta_i, \phi_i) = \frac{3}{4\pi\chi_{max}^3} \chi_i^2 \sin \theta_i \quad (\text{A4})$$

where χ_i, θ_i, ϕ_i are the spin vector's polar coordinates relative to the orbital angular momentum vector [77].

Beta function spin prior (precessing): More generally, we can adopt a Beta-distribution prior on the spin magnitude

$$p_\beta(\chi_i, \theta_i, \phi_i | p, q) = \frac{\Gamma(2 + p + q)}{\Gamma(1 + a)\Gamma(1 + b)} \frac{\chi_i^p (\chi_{max} - \chi_i)^q}{4\pi\chi_{max}^{p+q+1}} \sin \theta_i \quad (\text{A5})$$

In this representation, the volumetric spin prior corresponds to $p = 2, q = 0$. The default prior adopted by LIGO when inferring BH spins uses a uniform spin magnitude distribution [9], corresponding to $p = q = 0$:

$$p_{umag}(\chi_i, \theta_i, \phi_i) = \frac{1}{4\pi\chi_{max}} \sin \theta_i \quad (\text{A6})$$

Aligned spin: When both spins must be parallel to the orbital angular momentum, by default we employ a uniform prior on $\chi_{i,z} \in [-\chi_{max}, \chi_{max}]$. To enable comparison to precessing LIGO results, we also employ an alternative prior (“zprior”), proposed by Veitch [78]

$$p_{zprior}(\chi_{i,z}) = \frac{1}{2\chi_{max}} (-\ln |\chi_{i,z}/\chi_{max}|) \quad (\text{A7})$$

which is equivalent to the uniform spin magnitude prior after marginalizing out other degrees of freedom. To demonstrate that p_{zprior} is the corresponding marginal distribution of Eq. (A6), we perform the marginal integral, for convenience denoting spin components for convenience by x, y, z and χ_{max} by R . The cumulative distribution $P(< z)$ can be evaluated by the following expression when $z < 0$:

$$P(< z) = \int_{<z} \frac{dr d\phi d\cos\theta}{R 4\pi} \quad (\text{A8})$$

$$= \frac{1}{2R} \int_{-1}^{|z|/R} d\cos\theta \int_{|z|/|\cos\theta|}^R d\cos\theta \quad (\text{A9})$$

$$= \frac{1}{2R} [z + R - z \ln |z/R|] \quad (\text{A10})$$

and the result follows by differentiation.

Correlated, separable spin priors: In almost all cases, the posterior distribution tightly constrains χ_{eff} [Eq. (2)] but leaves the complementary degree of freedom almost completely unconstrained. To accelerate sampling in the common case with $m_1 \simeq m_2$, we can adopt a uniform spin prior in $\chi_{z,\pm} = (\chi_{1,z} \pm \chi_{2,z})/2$, then eliminate samples which have $\chi_{z,i}$ otherwise inconsistent with the limit imposed by χ_{max} . This approach can be directly employed to accelerate sampling with both the aligned uniform spin prior and the precessing volumetric prior; results for non-separable priors follow by reweighting posterior samples.

Marginal prior for χ_{eff} (uniform): Because the individual spin components $\chi_{i,z}$ are rarely observationally accessible, one can imagine marginalizing out the superfluous

degree of freedom, reducing the marginal likelihood and related Monte Carlo calculations to integrals like $I = \int_{|\chi_1|, |\chi_2| < 1} f(\chi_{\text{eff}}) d\chi_{1,z} d\chi_{2,z}$ via

$$I = \int f(\chi_{\text{eff}}) d\chi_1 d\chi_2 = 4 \int f(\chi_{\text{eff}}) p(\chi_{\text{eff}}|q) d\chi_{\text{eff}} \quad (\text{A11})$$

where for simplicity we adopt a uniform spin magnitude prior. This expression is not directly applicable to our low-level Monte Carlo technique, as this spin prior depends on mass ratio. Such an expression will however be a useful reference when we want to rescale posterior samples to alternative prior distributions.

Reweighting is only successful if the posterior has broad support. For nonprecessing inference, while analyses performed with Eq. (A7) generally have support concentrated near to zero spin, an analysis with the uniform spin magnitude prior will have support generally for all $\chi_{i,z}$ consistent with the likelihood. When constructing a fiducial marginal χ_{eff} distribution, we therefore derive it under the assumption of uniformly distributed $\chi_{i,z} \in [-\chi_{\text{max}}, \chi_{\text{max}}]$. In the interests of clarity and without loss of generality – all results scale linearly with χ_{max} – in the derivation that follows we adopt $\chi_{\text{max}} = 1$.

To evaluate $p(\chi_{\text{eff}}|q)$, we first define a helpful shorthand (to avoid ambiguity)

$$g(a, b) = \frac{m_1 a + m_2 b}{m_1 + m_2} = (a + qb)/(1 + q) \quad (\text{A12})$$

3. Tides

The tidal deformability of each compact binary can be characterized by a dimensionless parameter Λ_i , which is zero for black holes. By default, we adopt a uniform prior on $\Lambda_i \in [0, \Lambda_{\text{max}}]$.

The leading-order effects of tidal deformation enter into the gravitational wave signal via two quantities $\tilde{\Lambda}$, $\delta\tilde{\Lambda}$

$$\begin{aligned} \tilde{\Lambda} &= \frac{16}{13} \frac{(m_1 + 12m_2)m_1^4 \Lambda_1 + (m_2 + 12m_1)m_2^4 \Lambda_2}{(m_1 + m_2)^5} \\ &= \frac{8}{13} \left[(1 + 7\eta - 31\eta^2)(\Lambda_1 + \Lambda_2) + \sqrt{1 - 4\eta}(1 + 9\eta - 11\eta^2)(\Lambda_1 - \Lambda_2) \right] \end{aligned} \quad (\text{A18})$$

$$\delta\tilde{\Lambda} = \frac{1}{2} \left[\sqrt{1 - 4\eta} \left(1 - \frac{13272}{1319} \eta + \frac{8944}{1319} \eta^2 \right) (\Lambda_1 + \Lambda_2) + \left(1 - \frac{15910}{1319} \eta + \frac{32850}{1319} \eta^2 + \frac{3380}{1319} \eta^3 \right) (\Lambda_1 - \Lambda_2) \right], \quad (\text{A19})$$

In most cases of current astrophysical interest, $\tilde{\Lambda}$ can be weakly constrained and $\delta\tilde{\Lambda}$ cannot be constrained at all.

Because of the constraint that $\Lambda_i \geq 0$, a corner in tidal parameter space, the marginal distribution of $\tilde{\Lambda}$, $\delta\tilde{\Lambda}$ near $\tilde{\Lambda} \simeq 0$ increases linearly with $\tilde{\Lambda}$. To more transparently reflect the astrophysical significance of the posterior distribution of $\tilde{\Lambda}$, it is helpful to adopt a prior corresponding to a *uniform* distribution of $\tilde{\Lambda}$. Once again, such an alternative prior depends on binary mass ratios and therefore is useful only for post-processing and reweighting, not as part of our initial Monte Carlo analysis which requires separable priors. The underlying calculation of the marginal prior on $\tilde{\Lambda}$ follows exactly like the calculation for χ_{eff} above.

Appendix B: Supplementary validation studies of iterative posterior generation

In this section we describe systematic tests of the general algorithm and specific implementation described in Section

which is χ_{eff} . The integrand and prior has four natural break-points at $g(\pm 1, \pm 1)$, ordered so $g(-1, -1) \leq g(-1, 1) \leq g(1, -1) \leq g(1, 1)$. Within each region, we can do the integral $\int d\chi_1 d\chi_2 \delta(z - g(\chi_1, \chi_2))$ simply by keeping track of the limits of integration:

$$J(z) = \int_{-1}^1 d\chi_1 \int_{-1}^1 d\chi_2 \delta(z - g(\chi_1, \chi_2)) \quad (\text{A13})$$

$$= \int_{\chi_2 = \chi_2(\chi_1, \chi_{\text{eff}})} d\chi_1 (1 + q)/q \quad (\text{A14})$$

$$= \frac{(1 + q)}{q} [\chi_{1,+} - \chi_{1,-}] \quad (\text{A15})$$

where $\chi_{1,\pm}$ are the largest and smallest allowed values of χ_1 for a given choice of χ_{eff} . Looking at the square, when $\chi_{\text{eff}} < g(-1, 1)$, we know $\chi_{1,-} = -1$ and when $\chi_{\text{eff}} > g(1, -1)$ we know the upper bound is 1. Otherwise, we know $\chi_{1,\pm}$ occurs when $\chi_2 = \pm 1$, implying

$$\chi_{1,\pm}(z) = \pm q + z(1 + q) \quad (\text{A16})$$

We find the following expression for our marginal prior

$$p(z|q) = \frac{1 + q}{4q} \times \begin{cases} 1 - \chi_{1,-} & z \in [g(1, -1), g(1, 1)] \\ \chi_{1,+} - \chi_{1,-} = 2q & z \in [g(-1, 1), g(1, -1)] \\ \chi_{1,+} + 1 & z \in [g(-1, -1), g(-1, 1)] \end{cases} \quad (\text{A17})$$

II to reconstruct the posterior distribution by means of iteratively fitting the likelihood distribution, then drawing candidate points from the posterior distribution.

In these controlled tests, we generate synthetic likelihood

function on a hypercube $x \in [-1, 1]^d$ and a gaussian mixture model:

$$\mathcal{L}(x) = \mathcal{L}_{\text{ref}} p(x) = \mathcal{L}_{\text{ref}} \sum_k \frac{w_k}{(2\pi\sigma^2)^{d/2}} e^{-(x-\mu_k)^2/2\sigma^2} \quad (\text{B1})$$

where w_k are weights with $\sum_k w_k = 1$. We drew random weights; random gaussian centers μ_k in the hypercube $[-0.6, 0.7]/\sqrt{d}$; and for convenience fixed $\sigma = 0.1$. We drew initial points randomly from the hypercube, seeded by a few points from the true posterior distribution, then applied our iterative code, iterating five times. Figure 10 shows an example of the output of our code, compared to the analytic one- and two-dimensional posterior distributions for a generic three-dimensional and four-component gaussian mixture model. To quantify agreement between the two distributions, we also provide an (approximate) KL divergence $\int dz p_1(z) \ln p_1(z)/q_1(z)$, where $p_1(z)$ is the exact 1d marginal distribution and $q_1(z)$ is our approximate 1d marginal distribution. A fairly accurate reconstruction will have $D_{KL} \lesssim 2 \times 10^{-2}$. For arbitrary gaussian mixture models in dimensions $d \leq 6$, we confirmed our approach consistently reproduces one- and two-dimensional posterior marginal distributions, with small error.

Appendix C: Evaluating the evidence for an equation of state

In Section VD we described a simple integral over source intrinsic parameters and redshift [Eq. (11)] to assess the com-

patibility with a given observation and a proposed equation of state, characterized by hyper-parameters γ which determine a relationship between tidal deformability λ and source-frame NS gravitational mass m : $\lambda = \lambda(m|\gamma)$. Because GW measurements naturally very tightly constrain the redshifted chirp mass $\mathcal{M}_z = \mathcal{M}(1+z)$ to a characteristic range of scale $\sigma_{\mathcal{M}_z}$, the integrand is nearly zero except for a very narrow range of \mathcal{M}_z centered on $\mathcal{M}_{z,*}$. Additionally, to an excellent approximation the integrand does not depend on $\delta\tilde{\Lambda}$, and the function $\lambda(m)$ is effectively constant when the mass changes by of order $\sigma_{\mathcal{M}_z}$. We therefore change variables to $\mathcal{M}_z, \eta, z, \chi_i$ [Eq. (A1)], then perform the integral over \mathcal{M}_z and χ_i :

$$I(\gamma) = \int dz d\eta \frac{4p(z|\mathcal{M}_{z,*})G(\eta, \tilde{\Lambda}(\eta, \mathcal{M}_{z,*}))}{(1+z)^2 (M_{max} - m_{min})^2 \eta^{6/5} \sqrt{1-4\eta}} \quad (\text{C1})$$

$$G(\eta, \tilde{\Lambda}) = \int d\mathcal{M} \mathcal{M} \mathcal{L}(\mathcal{M}, \eta, \tilde{\Lambda}) d\chi_1 d\chi_2 p(\chi_1, \chi_2) \quad (\text{C2})$$

where $\tilde{\Lambda}_*(\eta, z)$ follows by evaluating $\lambda_i(m_i)$ using the masses m_i derived from η and the appropriate source-frame chirp mass $\mathcal{M}_{z,*}/(1+z)$, and where $p(z|\mathcal{M}_{z,*})$ is the fully marginalized distance distribution implied by this observation for a source with detector-frame chirp mass $\mathcal{M}_{z,*}$. Following Eq. (A2), changing coordinates to δ rather than η removes the integrable singularity at $\eta = 1/4$ and makes numerical methods more robust.

-
- [1] B. Abbott et al. (The LIGO Scientific Collaboration). Advanced LIGO. *Class. Quant. Grav.*, 32(7):074001, April 2015.
 - [2] T. Accadia and et al. Virgo: a laser interferometer to detect gravitational waves. *Journal of Instrumentation*, 7(03):P03012, 2012.
 - [3] The LIGO Scientific Collaboration and the Virgo Collaboration. Direct Observation of Gravitational Waves from a Binary Black Hole Merger. *Phys. Rev. Lett.*, 16:061102+, February 2016.
 - [4] B. Abbott et al. (The LIGO Scientific Collaboration and the Virgo Collaboration). Binary black hole mergers in the First Advanced LIGO observing run. *Phys. Rev. X*, 6:041015, October 2016.
 - [5] B. P. Abbott, R. Abbott, T. D. Abbott, F. Acernese, K. Ackley, C. Adams, T. Adams, P. Addesso, R. X. Adhikari, V. B. Adya, and et al. GW170104: Observation of a 50-Solar-Mass Binary Black Hole Coalescence at Redshift 0.2. *Physical Review Letters*, 118(22):221101, June 2017.
 - [6] The LIGO Scientific Collaboration, the Virgo Collaboration, B. P. Abbott, R. Abbott, T. D. Abbott, F. Acernese, K. Ackley, C. Adams, T. Adams, P. Addesso, R. X. Adhikari, V. B. Adya, and et al. GW170814: A Three-Detector Observation of Gravitational Waves from a Binary Black Hole Coalescence. *Physical Review Letters*, 119(14):141101, October 2017.
 - [7] The LIGO Scientific Collaboration, the Virgo Collaboration, B. P. Abbott, R. Abbott, T. D. Abbott, F. Acernese, K. Ackley, C. Adams, T. Adams, P. Addesso, R. X. Adhikari, V. B. Adya, and et al. GW170608: Observation of a 19 Solar-mass Binary Black Hole Coalescence. *Astrophysical Journal*, 851:L35, December 2017.
 - [8] The LIGO Scientific Collaboration, the Virgo Collaboration, B. P. Abbott, R. Abbott, T. D. Abbott, F. Acernese, K. Ackley, C. Adams, T. Adams, P. Addesso, and et al. GW170817: Observation of gravitational waves from a binary neutron star inspiral. *Phys. Rev. Lett.*, 119:141101, October 2017.
 - [9] J. Veitch, V. Raymond, B. Farr, W. M. Farr, P. Graff, S. Vitale, B. Aylott, K. Blackburn, N. Christensen, M. Coughlin, W. D. Pozzo, F. Feroz, J. Gair, C. Haster, V. Kalogera, T. Littenberg, I. Mandel, R. O’Shaughnessy, M. Pitkin, C. Rodriguez, C. Röver, T. Sidery, R. Smith, M. V. D. Sluys, A. Vecchio, W. Vousden, and L. Wade. Robust parameter estimation for compact binaries with ground-based gravitational-wave observations using LALInference. *Phys. Rev. D*, 91:042003, Feb 2015.
 - [10] C. Pankow, P. Brady, E. Ochsner, and R. O’Shaughnessy. Novel scheme for rapid parallel parameter estimation of gravitational waves from compact binary coalescences. *Phys. Rev. D*, 92(2):023002, July 2015.
 - [11] B. Abbott et al. (The LIGO Scientific Collaboration and the Virgo Collaboration). Directly comparing GW150914 with numerical solutions of Einstein’s equations for binary black hole coalescence. *Phys. Rev. D*, 94:064035, June 2016.
 - [12] J. Lange, R. O’Shaughnessy, M. Boyle, J. Calderón Bustillo, M. Campanelli, T. Chu, J. A. Clark, N. Demos, H. Fong, J. Healy, D. A. Hemberger, I. Hinder, K. Jani, B. Khamesra,

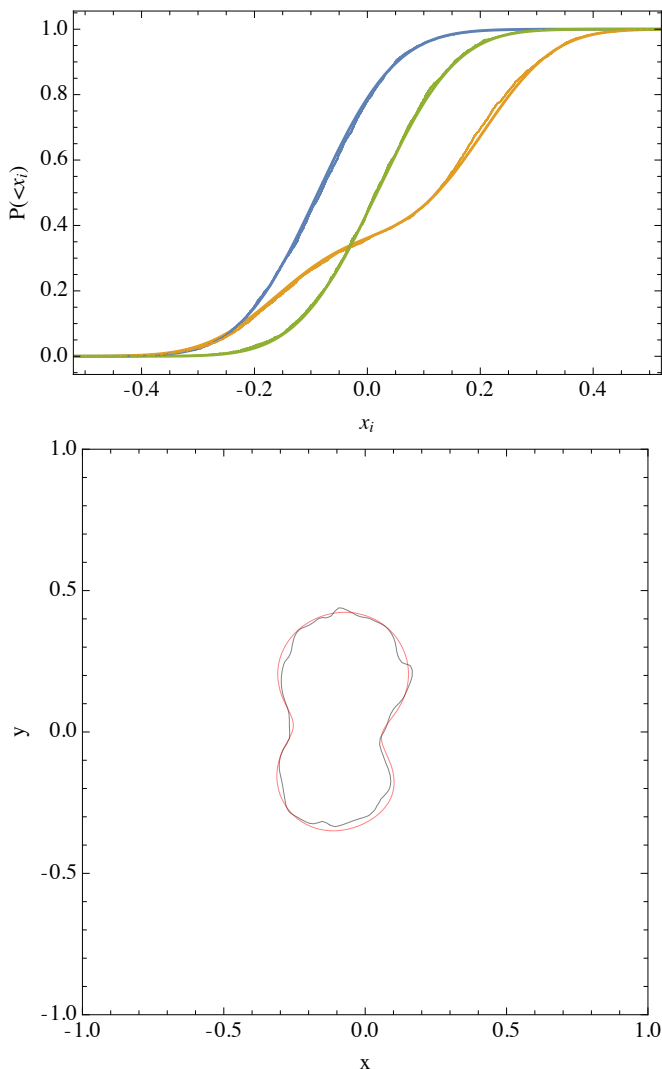


FIG. 10: **Reliable reconstruction in three dimensions:** Parameter inference of a 3 dimensional gaussian mixture model with 4 components, compared with the analytic posterior distribution. *Top panel:* The marginal, 1-dimensional posterior estimates extracted from a mixture of four randomly-centered 3-dimensional gaussians. Solid lines show the cumulative 1d distributions for each of the three dimensions; points show the estimated distributions from our code. The numbers on the left provide an (approximate) KL divergence between each marginal 1d distribution and the known 1d marginal distribution. The first number refers to the first (blue) curve, and so forth (yellow, green, . . .). *Bottom panel:* The 90% credible interval derived from the exact (red) and approximate (black) two-dimensional marginal distribution. The black curve is estimated based on 2000 samples drawn from the posterior distribution.

L. E. Kidder, P. Kumar, P. Laguna, C. O. Lousto, G. Lovelace, S. Ossokine, H. Pfeiffer, M. A. Scheel, D. M. Shoemaker, B. Szilágyi, S. Teukolsky, and Y. Zlochower. Parameter estimation method that directly compares gravitational wave observations to numerical relativity. *Phys. Rev. D*, 96(10):104041, November 2017.

[13] R. O’Shaughnessy, J. Blackman, and S. E. Field. An architecture for efficient gravitational wave parameter estimation with

multimodal linear surrogate models. *Classical and Quantum Gravity*, 34(14):144002, July 2017.

- [14] J. Lange, R. O’Shaughnessy, and M. Rizzo. Placement paper. 2017.
- [15] T. Damour. Coalescence of two spinning black holes: An effective one-body approach. *Phys. Rev. D*, 64(12):124013, December 2001.
- [16] É. Racine. Analysis of spin precession in binary black hole systems including quadrupole-monopole interaction. *Phys. Rev. D*, 78(4):044021, August 2008.
- [17] P. Ajith, M. Hannam, S. Husa, Y. Chen, B. Brügmann, N. Dorband, D. Müller, F. Ohme, D. Pollney, C. Reisswig, L. Santamaría, and J. Seiler. Inspiral-Merger-Ringdown Waveforms for Black-Hole Binaries with Nonprecessing Spins. *Physical Review Letters*, 106(24):241101, June 2011.
- [18] C.E. Rasmussen and C.I.K. Williams. *Gaussian Processes for Machine Learning*. The MIT Press, 2006.
- [19] R. van Haasteren and M. Vallisneri. New advances in the Gaussian-process approach to pulsar-timing data analysis. *Phys. Rev. D*, 90(10):104012, November 2014.
- [20] C. J. Moore and J. R. Gair. Novel Method for Incorporating Model Uncertainties into Gravitational Wave Parameter Estimates. *Physical Review Letters*, 113(25):251101, December 2014.
- [21] Z. Doctor, B. Farr, D. E. Holz, and M. Pürrer. Statistical gravitational waveform models: What to simulate next? *Phys. Rev. D*, 96(12):123011, December 2017.
- [22] C. J. Moore, C. P. L. Berry, A. J. K. Chua, and J. R. Gair. Improving gravitational-wave parameter estimation using Gaussian process regression. *Phys. Rev. D*, 93(6):064001, March 2016.
- [23] F. Pedregosa, G. Varoquaux, A. Gramfort, V. Michel, B. Thirion, O. Grisel, M. Blondel, P. Prettenhofer, R. Weiss, V. Dubourg, J. Vanderplas, A. Passos, D. Cournapeau, M. Brucher, M. Perrot, and E. Duchesnay. Scikit-learn: Machine learning in Python. *Journal of Machine Learning Research*, 12:2825–2830, 2011.
- [24] A. Taracchini, A. Buonanno, Y. Pan, T. Hinderer, M. Boyle, D. A. Hemberger, L. E. Kidder, G. Lovelace, A. H. Mroué, H. P. Pfeiffer, M. A. Scheel, B. Szilágyi, N. W. Taylor, and A. Zenginoglu. Effective-one-body model for black-hole binaries with generic mass ratios and spins. *Phys. Rev. D*, 89(6):061502, March 2014.
- [25] Y. Pan, A. Buonanno, A. Taracchini, L. E. Kidder, A. H. Mroué, H. P. Pfeiffer, M. A. Scheel, and B. Szilágyi. Inspiral-merger-ringdown waveforms of spinning, precessing black-hole binaries in the effective-one-body formalism. *Phys. Rev. D*, 89(8):084006, April 2014.
- [26] M. Hannam, P. Schmidt, A. Bohé, L. Haegel, S. Husa, F. Ohme, G. Pratten, and M. Pürrer. Simple Model of Complete Precessing Black-Hole-Binary Gravitational Waveforms. *Phys. Rev. Lett.*, 113(15):151101, October 2014.
- [27] J. Blackman, S. E. Field, C. R. Galley, B. Szilágyi, M. A. Scheel, M. Tiglio, and D. A. Hemberger. Fast and Accurate Prediction of Numerical Relativity Waveforms from Binary Black Hole Coalescences Using Surrogate Models. *Physical Review Letters*, 115(12):121102, September 2015.
- [28] J. Blackman, S. E. Field, M. A. Scheel, C. R. Galley, D. A. Hemberger, P. Schmidt, and R. Smith. A Surrogate model of gravitational waveforms from numerical relativity simulations of precessing binary black hole mergers. *Phys. Rev. D*, 95(10):104023, May 2017.
- [29] J. Blackman, S. E. Field, M. A. Scheel, C. R. Galley, C. D. Ott, M. Boyle, L. E. Kidder, H. P. Pfeiffer, and B. Szilágyi. Numer-

- ical relativity waveform surrogate model for generically precessing binary black hole mergers. *Phys. Rev. D*, 96(2):024058, July 2017.
- [30] A. Taracchini, Y. Pan, A. Buonanno, E. Barausse, M. Boyle, T. Chu, G. Lovelace, H. P. Pfeiffer, and M. A. Scheel. Prototype effective-one-body model for nonprecessing spinning inspiral-merger-ringdown waveforms. *Phys. Rev. D*, 86(2):024011, July 2012.
- [31] C. M. Will and A. G. Wiseman. Gravitational radiation from compact binary systems: Gravitational waveforms and energy loss to second post-Newtonian order. *Phys. Rev. D*, 54:4813–4848, October 1996.
- [32] L. E. Kidder. Coalescing binary systems of compact objects to (post)^{5/2}-Newtonian order. V. Spin effects. *Phys. Rev. D*, 52:821–847, July 1995.
- [33] Theocharis A. Apostolatos, Curt Cutler, Gerald J. Sussman, and Kip S. Thorne. Spin-induced orbital precession and its modulation of the gravitational waveforms from merging binaries. *Phys. Rev. D*, 49:6274, 1994.
- [34] Y. Pan, A. Buonanno, Y. Chen, and M. Vallisneri. A physical template family for gravitational waves from precessing binaries of spinning compact objects: Application to single-spin binaries. *Phys. Rev. D*, 69(10):104017–+, May 2004.
- [35] P. Schmidt, M. Hannam, S. Husa, and P. Ajith. Tracking the precession of compact binaries from their gravitational-wave signal. *Phys. Rev. D*, 84(2):024046, July 2011.
- [36] L. Pekowsky, R. O’Shaughnessy, J. Healy, and D. Shoemaker. Comparing gravitational waves from nonprecessing and precessing black hole binaries in the corotating frame. *Phys. Rev. D*, 88:024040, Jul 2013.
- [37] M. Boyle. Angular velocity of gravitational radiation from precessing binaries and the corotating frame. *Phys. Rev. D*, 87(10):104006, May 2013.
- [38] R. O’Shaughnessy, L. London, J. Healy, and D. Shoemaker. Precession during merger: Strong polarization changes are observationally accessible features of strong-field gravity during binary black hole merger. *Phys. Rev. D*, 87(4):044038, February 2013.
- [39] S. Ossokine, M. Boyle, L. E. Kidder, H. P. Pfeiffer, M. A. Scheel, and B. Szilágyi. Comparing post-Newtonian and numerical relativity precession dynamics. *Phys. Rev. D*, 92(10):104028, November 2015.
- [40] S. Babak, A. Taracchini, and A. Buonanno. Validating the effective-one-body model of spinning, precessing binary black holes against numerical relativity. *Phys. Rev. D*, 95(2):024010, January 2017.
- [41] A. Bohé, L. Shao, A. Taracchini, A. Buonanno, S. Babak, I. W. Harry, I. Hinder, S. Ossokine, M. Pürrer, V. Raymond, T. Chu, H. Fong, P. Kumar, H. P. Pfeiffer, M. Boyle, D. A. Hemberger, L. E. Kidder, G. Lovelace, M. A. Scheel, and B. Szilágyi. Improved effective-one-body model of spinning, nonprecessing binary black holes for the era of gravitational-wave astrophysics with advanced detectors. *Phys. Rev. D*, 95(4):044028, February 2017.
- [42] P. Ajith, S. Babak, Y. Chen, M. Hewitson, B. Krishnan, J. T. Whelan, B. Brügmann, P. Diener, J. Gonzalez, M. Hannam, S. Husa, M. Koppitz, D. Pollney, L. Rezzolla, L. Santamaría, A. M. Sintes, U. Sperhake, and J. Thornburg. A phenomenological template family for black-hole coalescence waveforms. *Classical and Quantum Gravity*, 24:689–+, October 2007.
- [43] L. Santamaría, F. Ohme, P. Ajith, B. Brügmann, N. Dorband, M. Hannam, S. Husa, P. Mösta, D. Pollney, C. Reisswig, E. L. Robinson, J. Seiler, and B. Krishnan. Matching post-Newtonian and numerical relativity waveforms: Systematic errors and a new phenomenological model for nonprecessing black hole binaries. *Phys. Rev. D*, 82(6):064016–+, September 2010.
- [44] S. E. Field, C. R. Galley, J. S. Hesthaven, J. Kaye, and M. Tiglio. Fast Prediction and Evaluation of Gravitational Waveforms Using Surrogate Models. *Physical Review X*, 4(3):031006, July 2014.
- [45] M. Pürrer. Frequency-domain reduced order models for gravitational waves from aligned-spin compact binaries. *Classical and Quantum Gravity*, 31(19):195010, October 2014.
- [46] B. D. Lackey, S. Bernuzzi, C. R. Galley, J. Meidam, and C. Van Den Broeck. Effective-one-body waveforms for binary neutron stars using surrogate models. *Phys. Rev. D*, 95(10):104036, May 2017.
- [47] R. Smith, S. E. Field, K. Blackburn, C.-J. Haster, M. Pürrer, V. Raymond, and P. Schmidt. Fast and accurate inference on gravitational waves from precessing compact binaries. *Phys. Rev. D*, 94(4):044031, August 2016.
- [48] É. É. Flanagan and T. Hinderer. Constraining neutron-star tidal Love numbers with gravitational-wave detectors. *Phys. Rev. D*, 77(2):021502, January 2008.
- [49] J. Vines, É. É. Flanagan, and T. Hinderer. Post-1-Newtonian tidal effects in the gravitational waveform from binary inspirals. *Phys. Rev. D*, 83(8):084051, April 2011.
- [50] T. Dietrich, S. Bernuzzi, and W. Tichy. Closed-form tidal approximants for binary neutron star gravitational waveforms constructed from high-resolution numerical relativity simulations. *Phys. Rev. D*, 96(12):121501, December 2017.
- [51] T. Dietrich, S. Khan, R. Dudi, S. Kapadia, P. Kumar, F. Ohme, A. Samajdar, F. Pannarale, S. Bernuzzi, G. Carullo, and et al. Augmenting binary-black-hole waveform models with numerical-relativity-tuned tidal effects. March 2018.
- [52] S. Bernuzzi, A. Nagar, T. Dietrich, and T. Damour. Modeling the Dynamics of Tidally Interacting Binary Neutron Stars up to the Merger. *Physical Review Letters*, 114(16):161103, April 2015.
- [53] A. Nagar, B. Bernuzzi, W. Del Pozzo, G. Reimensehneider, G. Carullo, S. Babak, K.W. Tsang, M. Colleoni, and et al. Time-domain effective-one-body gravitational waveforms for coalescing compact binaries with nonprecessing spins, tides and self-spin effects. Available at <https://dcc.ligo.org/LIGO-P1800141>, 2018.
- [54] T. Hinderer, A. Taracchini, F. Foucart, A. Buonanno, J. Steinhoff, M. Duez, L. E. Kidder, H. P. Pfeiffer, M. A. Scheel, B. Szilágyi, K. Hotokezaka, K. Kyutoku, M. Shibata, and C. W. Carpenter. Effects of Neutron-Star Dynamic Tides on Gravitational Waveforms within the Effective-One-Body Approach. *Physical Review Letters*, 116(18):181101, May 2016.
- [55] J. Steinhoff, T. Hinderer, A. Buonanno, and A. Taracchini. Dynamical tides in general relativity: Effective action and effective-one-body Hamiltonian. *Phys. Rev. D*, 94(10):104028, November 2016.
- [56] S. Marsat and J. Vines. SEOBNRv2T/v4T update: inclusion of quadrupole-monopole terms. *LIGO Technical Note T1800028*, available at <https://dcc.ligo.org/LIGO-T1800028>, January 2018.
- [57] E. Poisson. Gravitational waves from inspiraling compact binaries: The quadrupole-moment term. *Phys. Rev. D*, 57:5287–5290, April 1998.
- [58]
- [59] S. Nagar, S. Bernuzzi, and W. Del Pozzo. Effective-one-body model with spin and tidal interactions. *github*.
- [60] <http://www.black-holes.org/waveforms>.
- [61] A. H. Mroue, M. A. Scheel, B. Szilágyi, H. P. Pfeiffer, M. Boyle, D. A. Hemberger, L. E. Kidder, G. Lovelace, S. Os-

- sokine, N. W. Taylor, A. Zenginoglu, L. T. Buchman, T. Chu, E. Foley, M. Giesler, R. Owen, and S. A. Teukolsky. A catalog of 171 high-quality binary black-hole simulations for gravitational-wave astronomy. (*arXiv:1304.6077*), 2013.
- [62] J. Healy, C. O. Lousto, Y. Zlochower, and M. Campanelli. The RIT binary black hole simulations catalog. *Classical and Quantum Gravity*, 34(22):224001, November 2017.
- [63] Daniel Foreman-Mackey. corner.py: Scatterplot matrices in python. *The Journal of Open Source Software*, 24, 2016.
- [64] P. Kumar, T. Chu, H. Fong, H. P. Pfeiffer, M. Boyle, D. A. Hemberger, L. E. Kidder, M. A. Scheel, and B. Szilagyi. Accuracy of binary black hole waveform models for aligned-spin binaries. *ArXiv e-prints*, January 2016.
- [65] A. R. Williamson, J. Lange, R. O’Shaughnessy, J. A. Clark, P. Kumar, J. Calderón Bustillo, and J. Veitch. Systematic challenges for future gravitational wave measurements of precessing binary black holes. *Phys. Rev. D*, 96(12):124041, December 2017.
- [66] D. Wysocki, R. O’Shaughnessy, and J. Lange. Reconstructing phenomenological distributions of compact binaries via gravitational wave observations. *in prep*, 2018.
- [67] L. Lindblom. Spectral representations of neutron-star equations of state. *Phys. Rev. D*, 82(10):103011, November 2010.
- [68] L. Lindblom and N. M. Indik. Spectral approach to the relativistic inverse stellar structure problem II. *Phys. Rev. D*, 89(6):064003, March 2014.
- [69] A. Akmal, V. R. Pandharipande, and D. G. Ravenhall. Equation of state of nucleon matter and neutron star structure. *Phys. Rev. C*, 58:1804–1828, September 1998.
- [70] P. B. Demorest, T. Pennucci, S. M. Ransom, M. S. E. Roberts, and J. W. T. Hessels. A two-solar-mass neutron star measured using Shapiro delay. *Nature*, 467:1081–1083, October 2010.
- [71] J. Antoniadis, P. C. C. Freire, N. Wex, T. M. Tauris, R. S. Lynch, M. H. van Kerkwijk, M. Kramer, C. Bassa, V. S. Dhillon, T. Driebe, J. W. T. Hessels, V. M. Kaspi, V. I. Kondratiev, N. Langer, T. R. Marsh, M. A. McLaughlin, T. T. Pennucci, S. M. Ransom, I. H. Stairs, J. van Leeuwen, J. P. W. Verbiest, and D. G. Whelan. A Massive Pulsar in a Compact Relativistic Binary. *Science*, 340:448, April 2013.
- [72] M. Carney, L. Wade, and B. Irwin. Comparing two models for measuring the neutron star equation of state from gravitational-wave signals. Available at <https://dcc.ligo.org/LIGO-P1800126>, 2018.
- [73] M. Vallisneri, J. Kanner, R. Williams, A. Weinstein, and B. Stephens. The LIGO Open Science Center. In *Journal of Physics Conference Series*, volume 610 of *Journal of Physics Conference Series*, page 012021, May 2015.
- [74] The LIGO Scientific Collaboration and the Virgo Collaboration. GW150914: A merging binary black hole at redshift 0.1. Available at <https://dcc.ligo.org/LIGO-P1500218>, February 2016.
- [75] B. P. Abbott, R. Abbott, T. D. Abbott, M. R. Abernathy, F. Acernese, K. Ackley, C. Adams, T. Adams, P. Addesso, R. X. Adhikari, and et al. Improved Analysis of GW150914 Using a Fully Spin-Precessing Waveform Model. *Physical Review X*, 6(4):041014, October 2016.
- [76] B. P. Abbott, R. Abbott, T. D. Abbott, M. R. Abernathy, F. Acernese, K. Ackley, C. Adams, T. Adams, P. Addesso, R. X. Adhikari, and et al. Effects of waveform model systematics on the interpretation of GW150914. *Classical and Quantum Gravity*, 34(10):104002, May 2017.
- [77] B. Farr, E. Ochsner, W. M. Farr, and R. O’Shaughnessy. A more effective coordinate system for parameter estimation of precessing compact binaries from gravitational waves. *Phys. Rev. D*, 90(2):024018, July 2014.
- [78] J Veitch. Add option for volumetric spin priors. *Private communication*, January 2017.